MODELING, DESIGN, FABRICATION AND CHARACTERIZATION OF MINIATURIZED, HIGH-CURRENT HANDLING AND HIGH-EFFICIENCY INDUCTORS

A Dissertation
Presented to
The Academic Faculty

by

Teng Sun

In Partial Fulfillment
of the Requirements for the Degree
Doctor of Philosophy in the
School of Materials Science and Engineering

Georgia Institute of Technology
May, 2019

MODELING, DESIGN, FABRICATION AND CHARACTERIZATION OF MINIATURIZED, HIGH-CURRENT HANDLING AND HIGH-EFFICIENCY INDUCTORS

Approved by:

Dr. Rao R. Tummala, Advisor
School of Materials Science and Engineering
Georgia Institute of Technology

Dr. P. Markondeya Raj
School of Biomedical Engineering
Florida International University

Dr. Dong Qin
School of Materials Science and Engineering
Georgia Institute of Technology

Dr. Eric Vogel
School of Materials Science and Engineering
Georgia Institute of Technology

Dr. Hamid Garmestani
School of Materials Science and Engineering
Georgia Institute of Technology

Date Approved: December 6, 2018

ACKNOWLEDGEMENTS

First and foremost, I would like to thank my advisor, Prof. Rao Tummala, for giving me the opportunity to work in a unique research environment at the Georgia Tech Package Research Center (GT-PRC). His vision in electronic packaging helped in guiding my thesis and preparing for my future career. I would also like to express my sincere gratitude to my research mentors, Dr Raj and Dr. Himani, who have provided invaluable supports for my research. Last but not least, I would like to thank Prof. Dong Qin, Prof. Eric Vogel and Prof. Hamid Garmestani for being my committee and for their valuable suggestions and feedbacks.

It would be impossible to complete my experiments without amazing PRC staff. I would like to give my thanks to Chris White, Jason Bishop, Lila, Karen May, Patricia Allen, Brian McGalde and Chelsea Heath for maintaining all the tools, scheduling conference call, arranging visit of industrial members. I would also like to extend my thanks to our industrial members, Furukawa Yoshihiro (Nitto Denko), Tomonori Ogawa (AGC) and Shuihei Yamada (Murata) for their technical support for my research.

It is my greatest pleasure to work with knowledgeable and passionate colleagues in PRC. I learned a lot from them and extended my expertise beyond material science. I would like to pass my thanks to Dibyajat Mishar, Zihan Wu, Hao Lv, Jialing Tong, Atom Watanabe, Siddharth Ravichandran, Lee Haksun, Rui Zhang, Tailong Shi, Omakr Gupte, Grant Spurney and Pratik Nimbalkar.

Finally, I would like to thank my family and my loved ones for supporting me purse my goals.

TABLE OF CONTENTS

LIST OF TABLES

LIST OF FIGURES

SUMMARY

Power delivery is a key need that presents many challenges in all current and future electronic systems. It comprises of power storage and conversion, and power delivery through the low-impedance board, package and IC power distribution network. Power conversion close to the load, with high power conversion ratio from the high-voltage bus to the point-of-load, with minimal power conversion stages, and low active and passive component losses are the key requirements for efficient power conversion. Such approach minimizes package parasitics and reduces the needs for decoupling capacitors. Power component need vary based on the power requirements and converter topologies that are utilized for different applications such as high-performance computing (AI, servers, data center) and mobile computing. High-efficiency power converters are predominantly based on switching regulator topologies that utilize inductors or transformers as the main storage components. These components determine the size, efficiency, system integration and miniaturization options for both mobile and high-performance computing. Their low-power density which leads to large sizes has, however, been a major bottleneck for power module integration and efficient power management. High-density and miniaturized inductors can help migrate the power converters close to the processors. This can lead to lower losses, more efficient and granular power delivery. However, traditional magnetic materials that are used to fabricate inductors cannot achieve very high-power density or current-handling. Magnetic flake-composite materials provide unique opportunities to address these challenges by enhancing permeability, frequency stability, miniaturizing and integrating inductors close to the processor loads.

The primary objective of this research is to model, design and demonstrate miniaturized, high-efficiency and high-current handling power inductors with thickness of ~ 500 um, L/R_{DC} of 10 - 20 nH/mΩ and current handling of 1-2 A/mm^2. To achieve the specifications, this requires major advances in magnetic materials with permeabilities of ~141, high-frequency stability 10 MHz, scalability as well as specific inductor designs, materials, and innovative substrate-embedding processes and characterizations.

Two-dimensional magnetic flakes provide multiple degrees of freedom that can be optimized to achieve high in-plane permeability with large X-Y dimensions and low eddy current losses from small Z dimensions. The low eddy current losses make the flakes suitable for high-frequency applications. By synthesizing them as polymer composites, adequate thickness can be achieved for high current-handling. Advanced materials with 2D magnetic flakes are designed to achieve high in-plane permeability and high-frequency stability from their plate-like morphology. These materials are processed to achieve adequate thicknesses for current-handling. Such advanced materials are then integrated into inductors with innovative designs for achieving high-inductance density with low DC resistance or high L/R_{DC} value and high current-handling, with smaller footprints and lower thicknesses. Innovative material processing is developed to integrate such inductors with ultra-high performance into thin substrates.

CHAPTER 1. INTRODUCTION

1.1 Background

Increased power density with enhanced efficiency has been driving the need for improved power delivery and management in emerging electronic systems. Power modules such as voltage regulators (VRs) are incorporated between the power sources and device loads to up- or down-convert the voltages and regulate the power supply. These modules consist of a network of active components comprising of switches and drivers, and passives components such as capacitors and inductors to transfer power to the loads at the desired voltage levels. If the power modules are integrated with the processors, which act as the loads, they are referred to as integrated voltage regulators (IVRs).

Power modules are predominantly based on 2D architectures, where the components are surface-mounted onto printed circuit board (PCB), as shown in Figure 1.1(a). The passive components are designed with large footprints and thicknesses to handle the require currents because of their lower power efficiencies. The 2D architectures also lead to long interconnection lengths between the passive components and the loads such as ICs. Energy is dissipated when traveling though the long interconnection. This can lead to higher losses and poor efficiency. To address these challenges, companies such as TI and TDK migrated to 3D integration architectures where active components are embedded into substrates to lower the module size as shown in Figure 1.1(b) and Figure 1.2. TDK demonstrated 60% reduction in PCB foot-print with embedded active components [1]. However, embedded actives approach only results in limited advantages

in performance improvement and thickness reduction because the bulkier passive components are still surface-mounted onto the top of the packages.

In order to further lower the module size and improve the efficiency, passive components need to be integrated into the substrates with low profile at low cost, as shown in Figure 1.1(c). This can lead to lower losses and more efficient power delivery due to shorter interconnection lengths and lower parasitics. Advanced materials, passive component designs and innovative integration processes are required to realize the miniaturization of power modules and their heterogeneous package integration. This forms the main focus of this thesis.

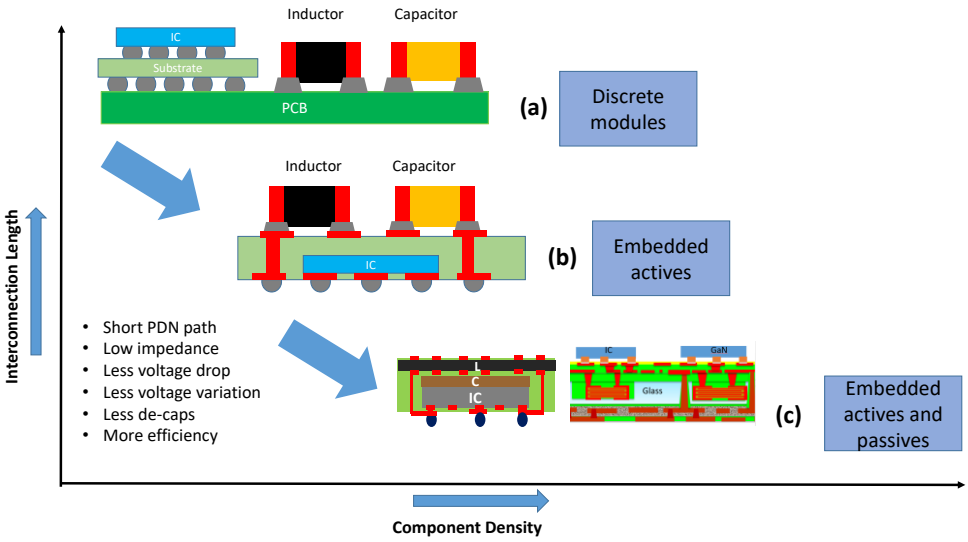

Figure 1.1: Technology trend to miniaturized and integrated power modules.

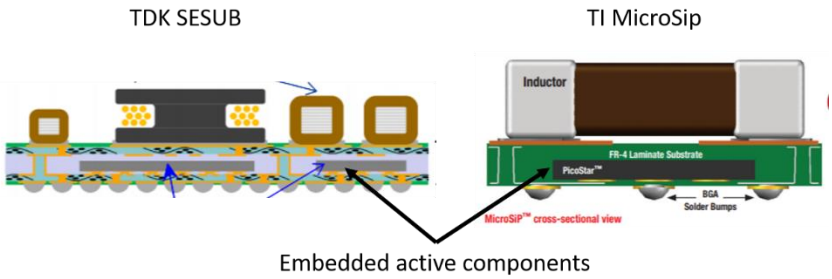

Figure 1.2: Cross-section of current substrates with embedded active components from TDK and TI.

In power modules with switching regulators or hybrid converter topologies, capacitors and inductors are the primary passive components in the modules. While several advances were reported in capacitor technologies to reduce the thickness profile for easier substrate integration, inductors have been lagging behind. Capacitor advances are briefly introduced in the first part of this section. Murata showed world's smallest discrete multi-layer co-fired ceramic (MLCC) capacitors. The LXFC series discrete MLCC capacitors have the lowest thickness profile of 50 μm. This allows the discrete capacitors to be picked and placed under the ICs as shown in Figure 1.3 to reduce package thickness [2]. Samsung has similar discrete capacitors with profile of 100 μm [3]. These MLCC discrete capacitors also have copper terminations that can form copper-via connections when integrated into substrates. The copper-via connections are compatible with substrate build-up process and can provide reliable connectivity.

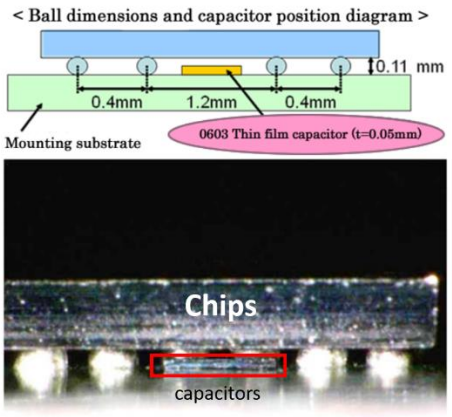

Figure 1.3: Murata's low-profile MLCC capacitors placed below ICs.

In addition to the discrete capacitors, capacitors can also be integrated into trenches in Si substrates using conformal dielectric deposition techniques such as thermal oxidation, chemical vapor deposition (CVD) and atomic layer deposition (ALD) technologies. By using alternating metal-dielectric-metal structure, IPDiA (currently, a part of Murata) integrated two parallelized capacitors into silicon trench, as shown in Figure 1.4a to achieve high capacitance. The trench capacitors also utilize tripod architecture instead of pore architecture for high surface area and high capacitance as shown in Figure 1.4 b and c[4]. Such capacitors have been reported to achieve densities of 0.2 microfarad/mm^2 are directly integrated onto silicon.

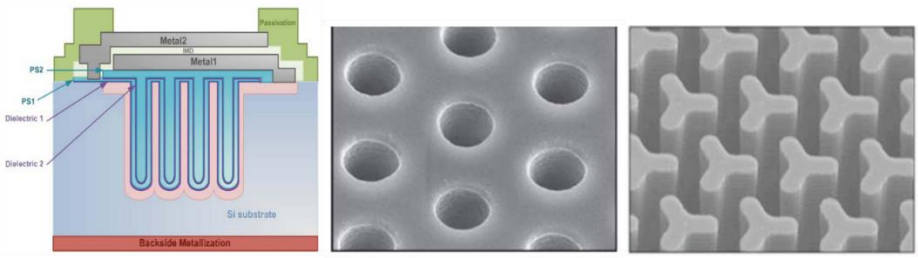

Figure 1.4: (a) IPDiA silicon trench capacitors (b) traditional Si Pores (trench) and (c) Tripod-based silicon trench architecture [4].

As compared to capacitors, there are not enough breakthrough technologies that enable the integration of high-performance inductors into substrates. The thinnest discrete power inductors from world leading passive components manufactures are 0.4 mm thick (Murata) and 0.5 mm thick (Coilcraft). The thickness profile is 10x thicker than the aforementioned 0.05 mm thick capacitors. Additionally, none of the discrete inductors have copper terminations, which creates additional processing and reliability challenges. When integrating into substrates, solder is required to form interconnections between the inductor terminations and the rest of circuits. This can lead to solder reliability issues. If the inductors have copper terminations, stable copper interconnections can be formed by using electroplating process which can lead to interconnections with high reliability. Figure 1.5 illustrates the discrete inductors with solder-based (a) and copper-based (b) terminations. The high profile together with non-Cu terminations prevent the discrete inductors to be integrated into substrates.

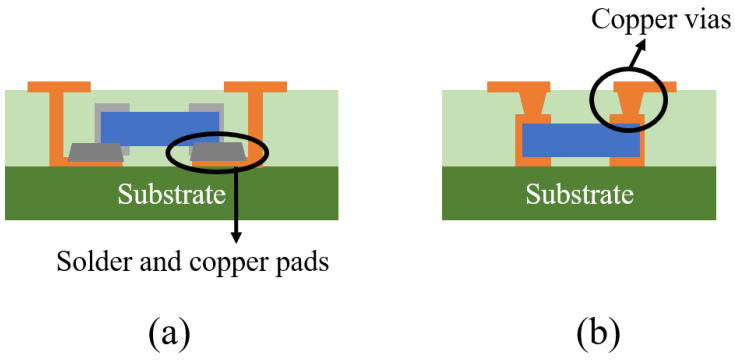

Figure 1.5: Illustration of inserted inductors with (a) solder-based terminations and (b) copper-based terminations.

Rather than integrating the discrete inductors into substrate to reduce power module size, inductors can be directly formed inside substrates to reduce power module size. These inductors are known as formed inductors. Intel has showed formed air-core inductors in substrates as shown in Figure 1.6 [5]. However, the air-core inductors have low inductance values, which can degrade the inductor performance. To achieve high inductance, large coil length or more number of copper windings are required, resulting in high DC resistance and low efficiency. Incorporation of high-permeability magnetic materials as inductor cores can enhance the inductance and reduce the need for the number of turns, thereby improving the inductor efficiency [2]. As shown in Murata's micro DC-DC converter in Figure 1.7, inductors are directly formed into ferrite substrates [6]. Magnetic flux is enhanced and concentrated by the ferrite substrates to give higher inductance to the inductors without the need for more winding turns.

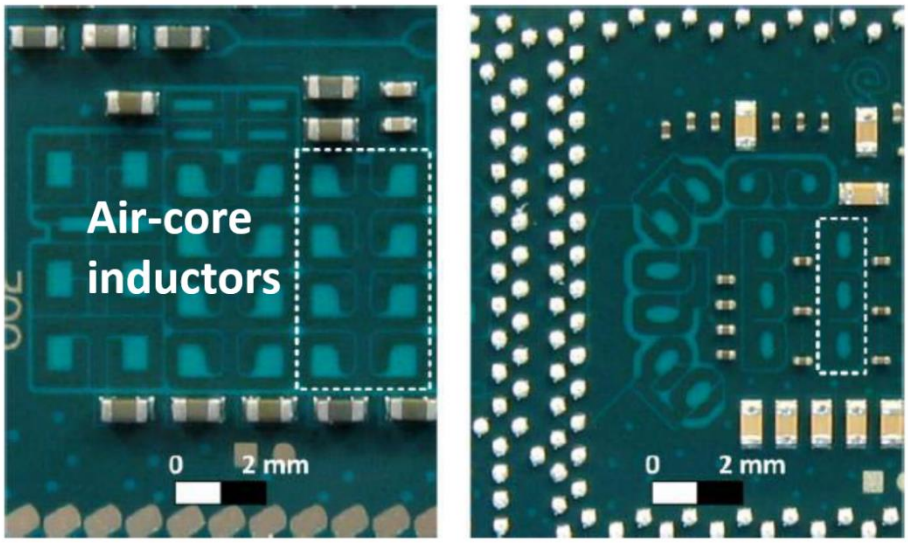

Figure 1.6: Integrated air-core inductors in processor packages [5].

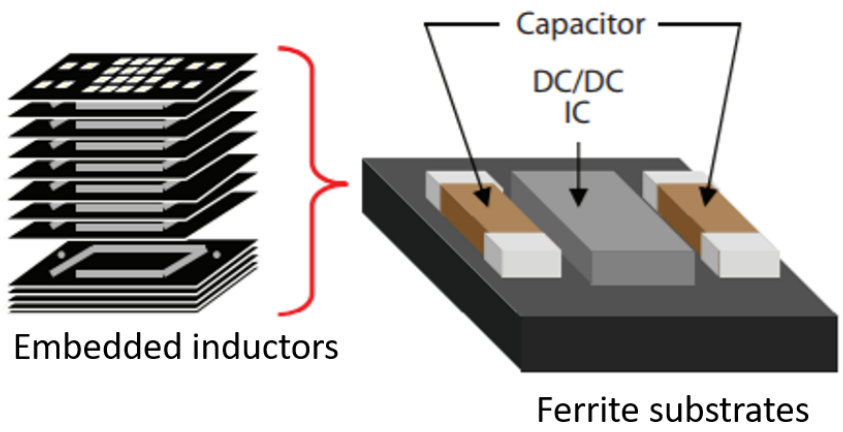

Figure 1.7: Integrated inductors in ferrite substrates.

Two major barriers are foreseen when incorporating magnetic materials as inductor cores. First concern is the frequency instability of magnetic materials. Figure 1.8 is a typical permeability spectrum as a function of frequency for various magnetic materials. Permeability has two parts, real permeability (μ') and imaginary permeability (μ''). The real part is related to the stored energy while the imaginary reflects the lost energy. There are two loss mechanisms, eddy current loss and ferromagnetic resonance loss. As the frequency increases, the losses further dominate, resulting in small real permeability and large imaginary permeability. When used as the inductor core, low real permeability and high imaginary permeability lead to low inductance and low inductor efficiency at high frequency. With the increased needs for higher operation frequency for switching power converters, high-frequency inductors with high inductance and high efficiency are needed.

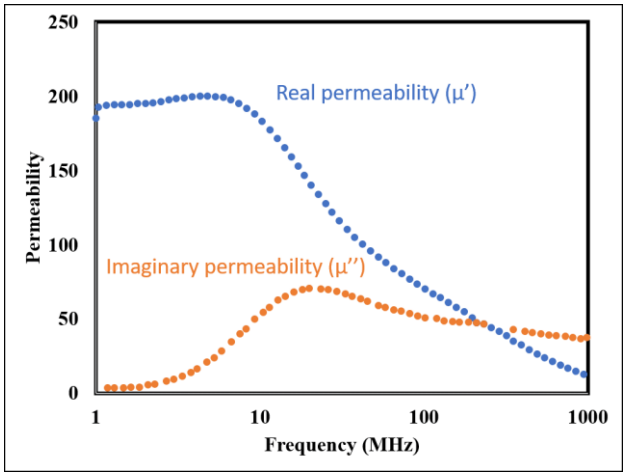

Figure 1.8: Typical complex permeability spectrum of magnetic materials

Second barrier is related to the magnetic saturation of the magnetic materials, which directly impacts the DC or AC current-handling and the power densities. Figure 1.9 (a) is an ideal hysteresis loop of magnetic materials with non-linear behavior. Under external applied magnetic field (H), magnetic materials are magnetized resulting in induced magnetic flux density (B) where increasing H field would lead to increase in B field. When the external field reaches the anisotropy field (H_k), further increase in H field would not lead to any further increase in B field. At that field, material is said to reach the saturation state. The magnetic flux at saturation is known as B_s (saturation magnetization). Since the permeability of magnetic materials is defined as $\mu=B_s/H_k$, the permeability decreases dramatically as the material approaches the saturation state. Figure 1.9 (b) shows the relation between permeability and H field.

The H field is generated when current running through the copper windings of inductors. Larger currents lead to stronger magnetic fields. With a stronger magnetic field, magnetic cores are saturated easily, resulting in small permeability and inductance. To avoid saturation, advanced inductor designs are needed.

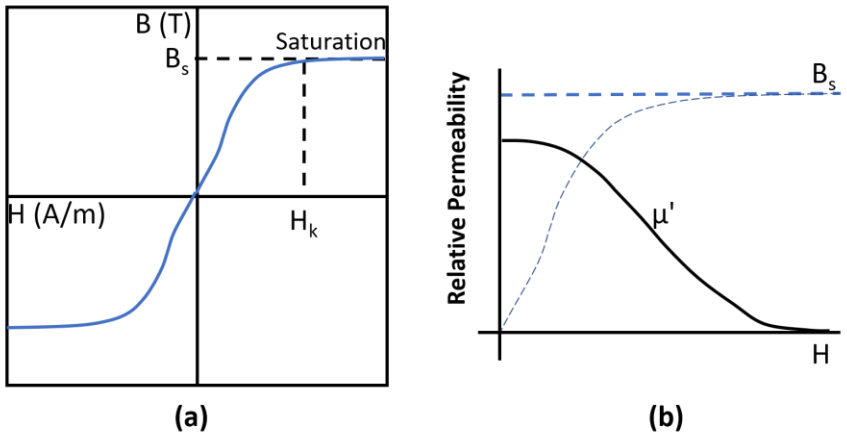

Figure 1.9: (a) B-H curve along the hard axis of magnetic materials and (b) Permeability and magnetization of magnetic cores as a function of magnetic field

1.2 Objectives

The research objective of this thesis is to design and demonstrate miniaturized inductors with high-current handling and high-efficiency for high frequency (1-10 MHz) applications. The targeted specifications are explained in the sub-section below and the key objectives with specified values are provided in Table 1.

Table 1: Specifications of the inductor in this research and the state-of-are inductors.

Objectives	Prior Art	Challenges	Tasks
Efficiency 10-20 nH/mΩ	5 - 20	Inadequate permeability leads to large coil length and high DC losses to high-inductance-density inductors	Model and design metal-polymer magnetic materials with high permeability

Current handling 1-2 A/mm^2	<0.5	High-density inductors with magnetic core saturate at low currents	Model and design Innovative topologies with high current-handling
Thickness 500 μm	500 - 1000	Lack of embedding process to integrate inductors into substrate to achieve miniaturization	Develop processes to integrate inductors into substrates

High Efficiency:

Motivation: As energy storage components, one of the critical parameters to evaluate the performance of inductors is their efficiency. For power inductors, the energy is stored in the magnetic field. The amount of stored energy can be calculated as

$$E = \frac{1}{2} L i^2 \tag{1.1}$$

where E is the stored energy, L is the inductance of inductor and i is the current traveling through the inductor. As indicated by Equation (1.1), inductors with high inductance can store more energy in their magnetic field. To achieve high inductance, inductors are designed to have large number of copper windings, which results in high DC resistance and DC loss. The AC losses are not considered in here since they can be controlled with interleaving power converters with multiphase switching topologies. This lowers the AC ripple current and suppresses the AC core losses. When DC current propagates though the copper windings, a significant fraction of energy is dissipated as heat due to the DC

resistance of copper. This leads to low efficiency to the inductors. Therefore, in order to accurately describe the efficiency of inductors, inductance per DC resistance (L/R_{DC}) is selected.

Challenges: High-permeability magnetic materials can be used as the cores of inductors to increase the inductance without increasing the number of copper windings. Therefore, a high L/R_{DC} value can be achieved. Most high-permeability magnetic materials for high-frequency applications are deposited by thin-film technologies such as PVD (Physical Vapor Deposition) and electroplating, which limit the thickness of the magnetic materials to be few microns. Due to the small thickness, these high-permeability magnetic materials are incompatible with technologies to form thick copper windings with low DC resistance. Eventually, the benefit brought by high-permeability magnetic materials is lost by the high DC resistance.

Certain magnetic materials such as ferrites can be made with thickness of hundreds of microns. The large thickness makes them compatible with technologies to form thick copper windings with low DC resistance. However, because of the ferromagnetic property, ferrites have low saturation magnetization (~ 0.5 T), and are not suitable for high-current handling. The other disadvantage of ferrites is their high-frequency instability. Most ferrites are only stable below 3 MHz, rendering them unsuitable for high-frequency application [7-9].

Task 1: Model and design thick magnetic composites with high permeability and high-frequency stability

- Magnetic materials will be developed by creating models to design the magnetic composites with desired structural and properties. Metal loading, particle shape and size etc. are some parameters that will be used to develop most suitable magnetic materials

High-Current Handling

Motivation: Current handling capacity is another critical parameter to judge the performance of power inductors. As load current increases in power applications such as DC-DC converters, the required inductance for power inductors decreases. The reduction of required inductance enables the reduction of inductor size to a point where the inductor size is compatible with processor size, rendering the possibility to integrate inductors with substrates. However, high-inductance-density inductors with magnetic cores tend to be saturated at high current, resulting in low permeability as described in Figure 1.9. Innovative inductor topologies are needed to avoid saturation of the magnetic cores.

Challenge: Various topologies such as stripline, spiral and solenoid are utilized for substrate-integrated inductors. The inductor topologies play an important role in determining the performance of inductors. Different topologies have their own advantages and disadvantages. For instance, spiral inductors have high L/R_{DC} but low-current handling. Solenoid inductors have low L/R_{DC} but high-current handling. Based on different applications and specifications, inductors need to be designed with different topologies. For magnetic cores with anisotropic properties, the permeability along certain directions is higher than other directions. In this case, the inductors need to be designed to only count for the high-permeability directions. Therefore, lack of suitable topologies for magnetic-

core inductors which have high-current handling, efficiency, inductance-density and small size simultaneously is the major challenge.

Task 2: Model and design magnetic-core inductors:

- Finite-element models will be built to design various inductor structures for high current handling of 1-2 A/mm^2, high efficiency of 10 - 20 nH/mΩ and low thickness of 500 μm.

Miniaturization

Motivation: The need for thinner inductors to realize miniaturized power modules sets up the stage for the third objective of this research. Substrate-integratable inductors with thickness around 500 μm are targeted. The specifications of targeted inductors and tabulated in Table 1. State-of-the art power inductors are in millimeter thicknesses due to the lack of suitable magnetic materials. These discrete inductors are surface-mounted on the substrates, occupying a large footprint and preventing system miniaturization. In addition, the long interconnection length between the discrete inductors and the ICs further increase the losses. With the trends to operate devices at high currents, the large interconnection length also leads to high DC resistance loss and low efficiency. Substrate-integrated inductors reduce the interconnect lengths to ICs, resulting in high efficiency and system miniaturization. The increasing needs for thin and substrate-integrated inductors is the main motivation for this research.

Challenges: Innovative embedding processes are needed to fabricate and integrate inductors into substrates. Fabrication and integration of the designed inductor with

advanced panel-scalable process remains a critical challenge to realize the inductor with desired attributes. One critical process step is to achieve conformal magnetic materials with copper traces. For thin copper traces, conformal integration can be easily realized. For high-efficiency inductors with low DC resistance, thick copper traces with high aspect ratio are used. Conformal magnetic films on such copper windings is a key process challenge. In addition to the conformal integration, forming high-aspect-ratio void-free copper traces [10] is another key challenge.

Task 3a: Develop and demonstrate innovative processes to fabricate and integrate the inductors into substrates

- Substrate-compatible processes such as panel lithography, electroplating and laser-drilling will be used to develop new embedding process to fabricate and integrate the inductors into substrates to realize system miniaturization. Critical process conditions such as lamination conditions and curing conditions will be optimized for different materials.

Task 3b: Characterize the fabricated inductors and validate the inductor designs

- Electrical characterization of the fabricated inductors will be performed. Inductance at various frequency and DC current ranges will be measured. The measured results will then be compared with simulation results to validate the inductor designs.

CHAPTER 2. LITERATURE REVIEW

This chapter starts with a review of the state-of-art magnetic materials for power inductors. The magnetic materials are classified into three categories based on their frequency stability.

Inductor topologies and their advantages and disadvantages are reviewed in the next part of the chapter. Magnetic-core inductors are classified into two types, MCM inductors and CMC inductors. For MCM inductors, copper windings are sandwiched between two magnetic layers. Similarly, for CMC inductors, the magnetic layers are sandwiched between two copper windings. Advantages and disadvantages for the two types of magnetic-core inductors are also discussed.

2.1 Magnetic Materials in Power Inductors

In general, the magnetic materials used for power applications such as transformers and inductors are classified into three categories based on their frequency stability. These are low (<5 MHz), medium (5 to 50 MHz) and high frequencies (50-150 MHz). Ferrites and metal ribbons are the major materials in low-frequency range. These materials are good for applications such as transformers. For medium frequencies, magnetic polymer composites are emerging as the major class of materials. For inductors at high frequencies, sputtered magnetic thin films are preferred.

2.1.1 Low-frequency Magnetic Materials

2.1.1.1 Ferrites

Soft ferrites have been widely used as the magnetic cores for low-frequency power applications such as transformers. They contain iron oxide (Fe_2O_3) in addition to other transition metals such as Mg, Mn, Zn and Ni [9]. Most soft ferrites for power applications have spinel structure ($MeFe_2O_4$), as shown in Figure 2.1. In the spinel structure, there are two sites in the cation sub-lattice, tetrahedral site (A-site) and octahedral site (B-site), where metal cations such as Me^{2+} and Fe^{3+} can occupy. The magnetic moments of cations in A-sites and B-sites are antiparallel to each other. Since there are as twice as many B-sites as A-sites, this lead to ferrimagnetic ordering to the spinel structure [11]. Because of this partial cancelation in magnetic moments, ferrites have lower saturation magnetization (<0.5 T) as compared to metal-based magnetic materials (~1 T) [7, 9, 12]. This limit them in the high-power applications. However, their magnetic softness and high resistivity make them attractive for inductor and transformer applications.

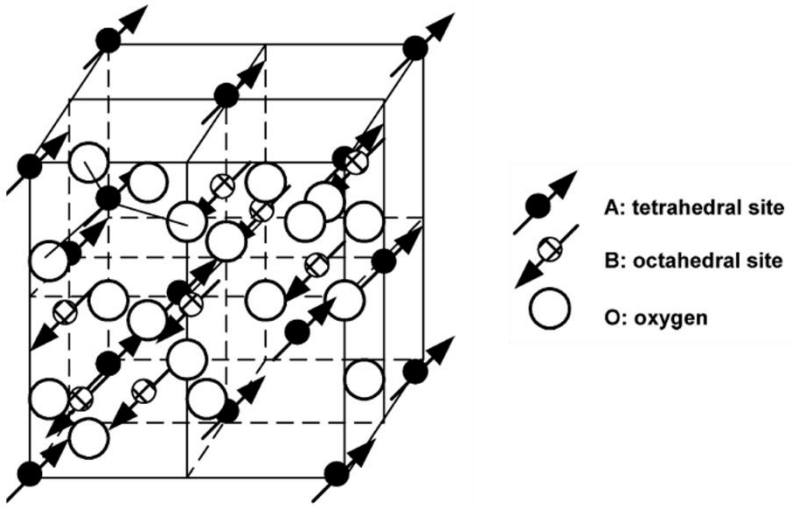

Figure 2.1: The unit cell structure of spinel ferrite.

Among all the ferrites, MnZn and NiZn ferrites are the most popular soft ferrites due to the good magnetic properties. Due to the high resistivity (> 1 Ω*m), these ferrites

result in low eddy current loss for thicker cores and are suitable for frequency upto 3 MHz without lamination, which is required for bulk metal cores [7-9].

Both MnZn and NiZn ferrites contain Zn ferrite, which has a normal spinel structure where Zn^{2+} occupies A-sites and Fe^{3+} occupies B-sites. Since Zn does not have unpaired electron in the out shell, this leads to a zero net magnetic moment in Zn ferrite. On the other hand, Mn ferrite has inverse spinel structure where A-sites are occupied by Fe^{3+} cations and B-sites are occupied by both Me^{2+} and Fe^{3+}. When zinc ion is added into Mn ferrite, it prefer to replace the Fe^{3+} at A-sites, resulting in an suppressed ferromagnetic cancellation and increase in net magnetic moment and in saturation magnetization. Similar phenomenon happens for NiZn ferrites [9, 13].

TDK Corporation showed new MnZn-based ferrite materials that are optimized for 700 kHz to 4 MHz frequency range. The MnZn based ferrites are suitable for fast-switching power supplies based on GaN. The Curie temperature of the ferrites is in excess of 250 ^{0}C, which make them stable in high-temperature environment [14]

2.1.1.2 Alloy Ribbons

Alloy ribbons are other material candidates for low-frequency power applications. As compared to ferrites, magnetic metals show higher saturation magnetization and higher permeability. The advanced properties enable miniaturization of transformers. However, the low conductivity of metal elements deteriorate the eddy current loss. To reduce eddy current losses, low-conductive elements such as Boron and Phosphorus are added to make magnetic metal-alloys such as Metaglass (FeSiBCuNb alloy) ribbon from Hitachi Metals, Ltd. [7, 15].

The technology to produce alloy ribbons is called rapidly-quenched casting. The process is shown in Figure 2.2. To produce amorphous alloys, the molten alloy must be quenched at a high rate of ~10^6 $^oC/s$. The rapid cooling does not give atoms enough time to rearrange into crystalline form, thus, leaving a metastable amorphous form [15]. The ribbons are then wound into toroid-shape magnetic cores. Due to the absence of grain boundaries and crystal magnetic anisotropy in amorphous alloys, amorphous alloys show better magnetic properties such as lower coercivity, higher permeability and lower core loss as compared to micro-crystalline alloys [15, 16]. To improve the magnetic properties, the amorphous alloys can be annealed under an external magnetic field at temperatures below the re-crystallization temperature. The internal stress caused by quenching is relieved at elevated temperatures resulting in better magnetic properties [17]. If heated above the re-crystallization temperature, large grains (~200 nm) in the comparable size as magnetic domain walls can form. These grains can pin the movement of domain wall during magnetization resulting in higher coercivity and higher core loss [18]. Other advantage of amorphous alloys is the high resistivity. Amorphous alloys usually have resistivity of 1.2 – 1.4 μΩm which is higher than corresponding crystalline magnetic materials with resistivity of 0.2 – 0.5 μΩm. The high resistivity allows the amorphous alloys to be used in few MHz frequencies [17].

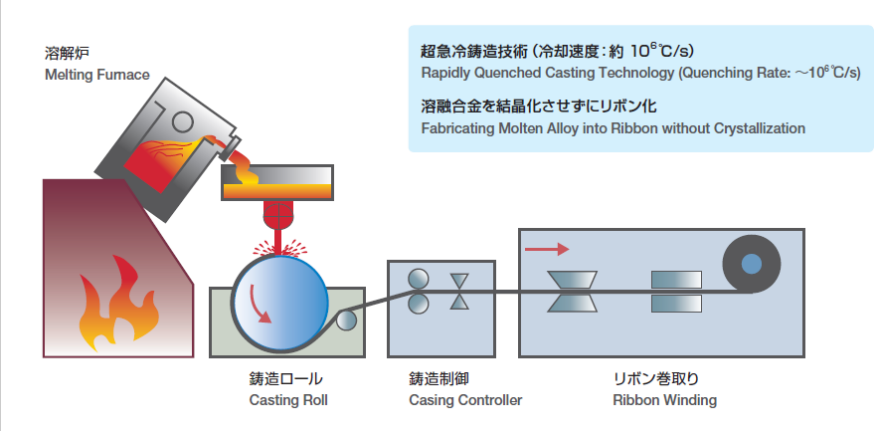

Figure 2.2: Process to produce amorphous alloy ribbons. [15]

2.1.2 Medium-frequency Magnetic Materials

2.1.2.1 Metal Power and Metal-Polymer Composite Cores

Metal-based particle or composite magnetic cores are suitable for medium-frequency applications. These composites consist of high permeability and high saturation magnetization (M_s) metal particles that are isolated by thin native oxides or polymer for low eddy current losses at high frequency. For applications where high DC-bias is constantly applied to the inductors, the high M_s prevent saturation of magnetic cores. The composites can easily be scaled to thick layers for high-current handling. Typical particle materials that are used in such cores are MPP, High Flux, Sendust and XFlux [9, 19].

MPP Core: MPP stands for molypermalloy powder. It consists of 81% nickel, 17% iron and 2% molybdenum. It has the lowest core losses as compared other powder cores. The MPP has several outstanding properties such as high resistivity, low hysteresis loss and eddy current loss. The cores are also stable under high DC-bias and high-temperature conditions.

High Flux Core: The High Flux core consists of 50% iron and 50% nickel. The core has the highest DC biasing capability as compared to other powder cores. The saturation magnetization of this core is ~1.5 T which is 2X higher than the MPP core and 3X higher than ferrites. The core is suitable for power applications with high DC bias and high AC ripple.

Sendust Core (Kool Mμ): The core consists of 85% iron, 9% silicon and 6% aluminum. Since there is no nickel in sendust core, it is cheaper and the production process is easier as compared to MPP and High Flux cores. The saturation magnetization of sendust core is ~1 T. As compared to ferrites, sendust core exhibit a soft saturation, which eliminates the complete collapse of inductance above a certain DC bias.

XFlux Core: The core consists of 6.5% silicon with the rest being iron. The core has lower losses as compared to pure iron powder and higher DC biasing capability. It has similar DC biasing capability as compared to High Flux core, making it a low-cost alternative to High Flux core. It also has soft saturation, which provides a design advantage. Table 2 lists the comparison between all the mentioned metal powder cores.

Table 2: Comparison of four magnetic powders

	MPP	High Flux	Kool Mμ®	XFlux®
Permeability	14-550	14-160	26-125	26-60
Core Loss	Lowest	Moderate	Low	High
Perm vs. DC Bias	Better	Best	Good	Best
Temperature Stability	Best	Very Good	Very Good	Good
Temperature Rating	200°C continuous	200°C continuous	200°C continuous	200°C continuous
Saturation Characteristic	Soft	Soft	Soft	Soft
Nickel Content	81%	50%	0%	0%
Relative Cost	High	Medium	Low	Low

2.1.2.2 Electroplated Films

Electroplated magnetic films are also used for medium frequency inductors. The films have high content of magnetic elements such as Fe and Ni that give high permeability and saturation magnetization [7]. NiFe thin-films have been used as the magnetic cores for on-chip inductors by Tydnall [20-22]. Figure 2.3 shows the cross-section of Tydnall's inductors with electroplated NiFe as the magnetic cores. Because of the small thickness of electroplated films, the inductors can only handle current up to 1 A [23]. Increasing the thickness of the films can lead to high-current handling at a cost of high-frequency instability due to eddy current loss.

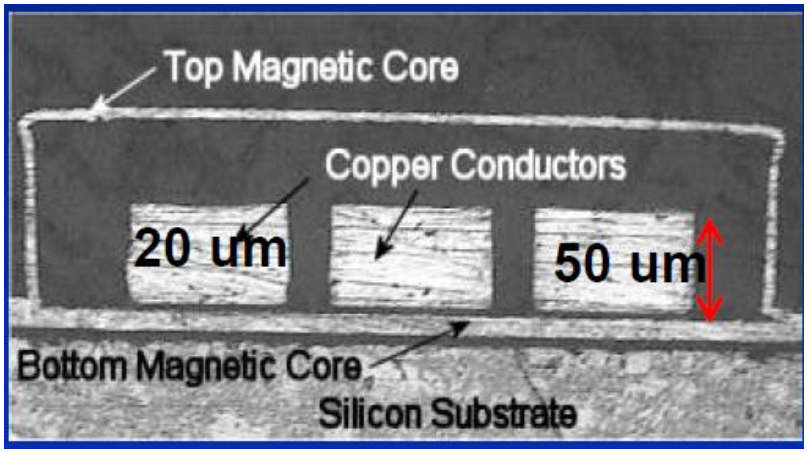

Figure 2.3: Cross-section of power inductors with electroplated NiFe films.

2.1.2.3 Metal Powders

Highly compacted metal powder cores are another candidate for power inductors [24]. Due to the high M_s of the metal powder, the cores can handle large current as compared to ferrite cores. Figure 2.4 shows inductance of two inductors with different magnetic cores. The inductors with metal-powder cores show stable inductance drop upto

8 A. The inductors with ferrite cores show significant drop in inductance at 2 A, indicating the low current-handling of ferrite cores. Since the metal powder is conductive, each powder is coated with a thin oxide layer to prevent electrical contact between the powders, rendering low eddy current losses and high-frequency stability. Figure 2.5 shows the SEM of metal powders coated with 100-200 nm thick oxide layers.

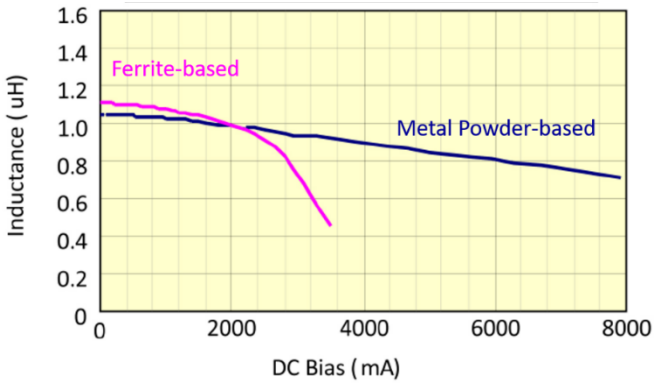

Figure 2.4: DC bias characterizations of metal powder-based and ferrite-based power inductors – source [24]

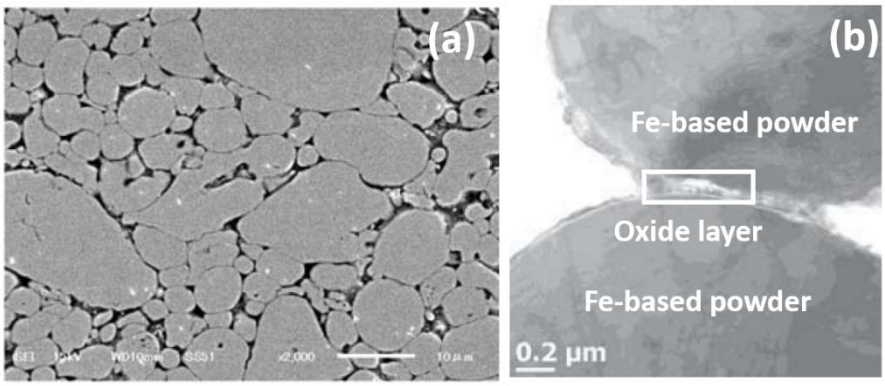

Figure 2.5: (a) SEM of the metal powders shows the absence of organic binder and (b) TEM image shows the thin oxide layer [24]

2.1.3 High-frequency magnetic cores

2.1.3.1 Sputtered Magnetic Thin-Films

Sputtered magnetic thin-films are widely used for high frequency applications because of their stable and high permeability above 100 MHz. For most magnetic materials, they obey Snoek's limit, which states that the product of ferromagnetic resonance (F_{res}) and relative permeability (μ_r) is proportional to the magnetization of materials as stated below.

$$(\mu_r - 1)F_{res} = \frac{\gamma}{3\pi} 4\pi M_s \tag{2.1}$$

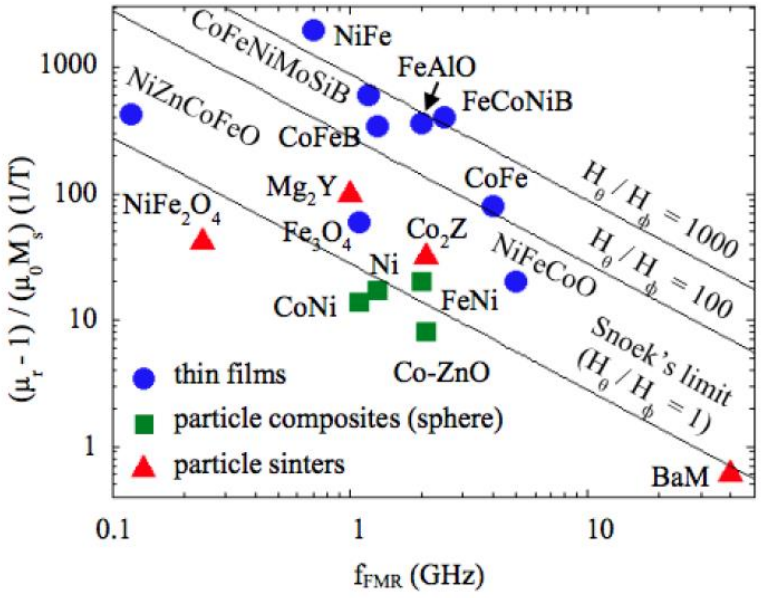

Figure 2.6: Illustration of snoek's limit and thin-films materials which extend the limit [25].

This imposes a limit on the high-frequency permeability values [26-28]. For sputtered magnetic thin-films, the Snoek's limit can be extended to allow high permeability at high frequency ranges as shown in Equation (2.1) [27].

Several sputtered thin-films such as NiFe [29] and CoZrTa [30] are used for inductor cores. The thin films have high content of magnetic elements such as Fe, Ni and Co that give high permeability and high saturation magnetization [7]. However, because of the high conductive elements (Ni and Fe), the thin-films generate high eddy currents at high frequency, which limits the applications of the films. To reduce the eddy current losses, low-conductivity elements such as B, P and O can be introduced into the films such as FeBN [31] and CoZrO [32]. The eddy current losses can also be limited by alternately laminating magnetic films and insulation films as demonstrate in [7, 29, 32]. Intel sputtered ~ 400 nm NiFe layer and ~ 10 nm insulation layer alternatively to form an 8-layer magnetic core to reduce eddy current loss as shown in Figure 2.7 [29].

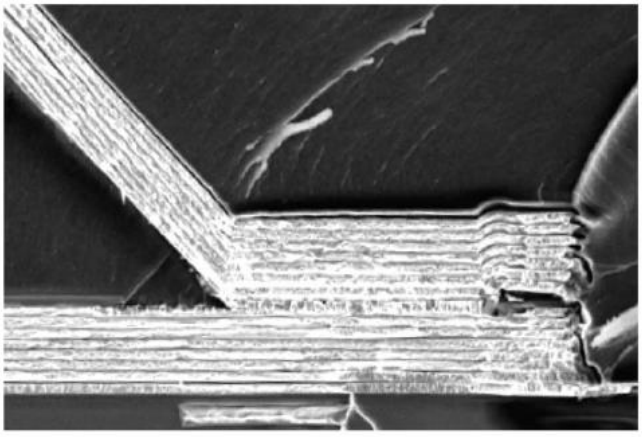

Figure 2.7: Laminated 8-layer NiFe magnetic core from Intel [29].

Since the thin-films are deposited with low throughput technologies such as PVD (physical vapor deposition), the thickness of the films is limited to few microns. This leads

to low-current handling (<1 A) for power inductors with thin-films as the magnetic cores [33].

By using the standard CMOS manufacturing processes, magnetic inductors with small profile can be integrated with CMOS ICs using back-end compatible process options [34]. Ferric, Inc demonstrated magnetic thin-film inductors that are integrated into the ICs, as shown in Figure 2.8. The inductors allow a shorter path for the power to be delivered to the ICs, resulting in a lower I^2R loss. The magnetic materials in the inductors are made of amorphous cobalt alloy with low coercivity (< 1 Oe) and high saturation field (~ 25 Oe). The magnetic films are separated by thin insulation layers, as shown in Figure 2.9, in order to to suppress eddy current loss. The multilayered magnetic films show high permeability of 600 up to 100 MHz. Inductors with the films as magnetic cores show stable inductance until 100 MHz as shown in Figure 2.10 [34].

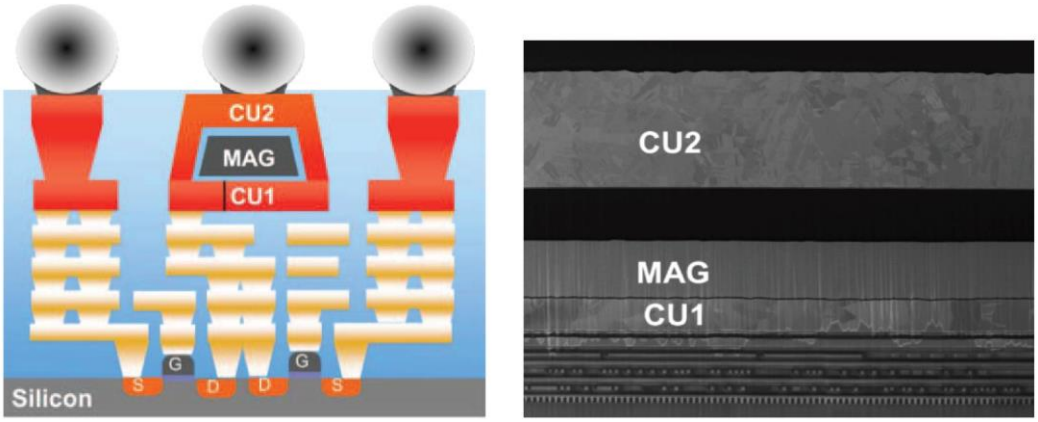

Figure 2.8: Left: Illustration of magnetic thin-film inductors integrated with ICs; Right: SEM cross-section of magnetic thin-film inductors integrated with ICs[34].

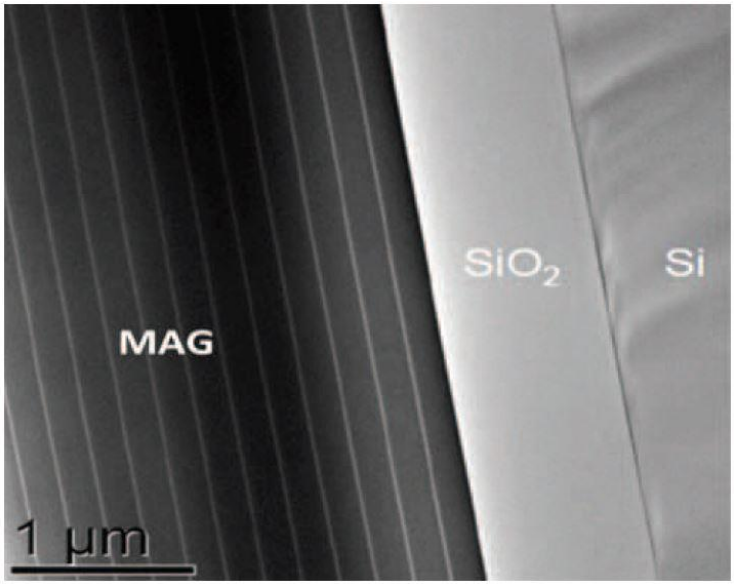

Figure 2.9: SEM of multilayered magnetic films [34].

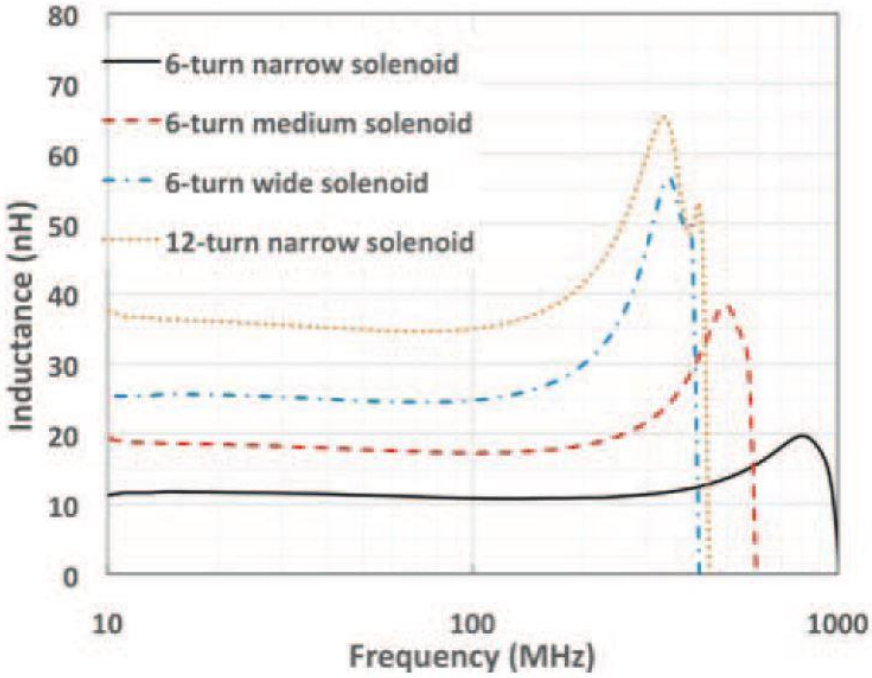

Figure 2.10: Inductance of magnetic thin-film inductors [34].

2.2 Inductor Topologies

Based on how the magnetic cores are integrated with copper windings, magnetic-core inductors are categorized into two types. One is Magnetic-Copper-Magnetic (MCM) inductor where copper windings are sandwiched between two magnetic layers. Strip-line and spiral inductors come in this category. The other type is Copper-Magnetic-Copper (CMC) inductors, where the magnetic cores are enclosed within the copper windings. Toroids and solenoid inductors come in this category. Figure 2.11 illustrates the difference between MCM and CMC inductors. Figure 2.12 show the schematics of all major types of magnetic core inductors.

Figure 2.11: Cross-sections illustrate the difference between MCM and CMC inductors

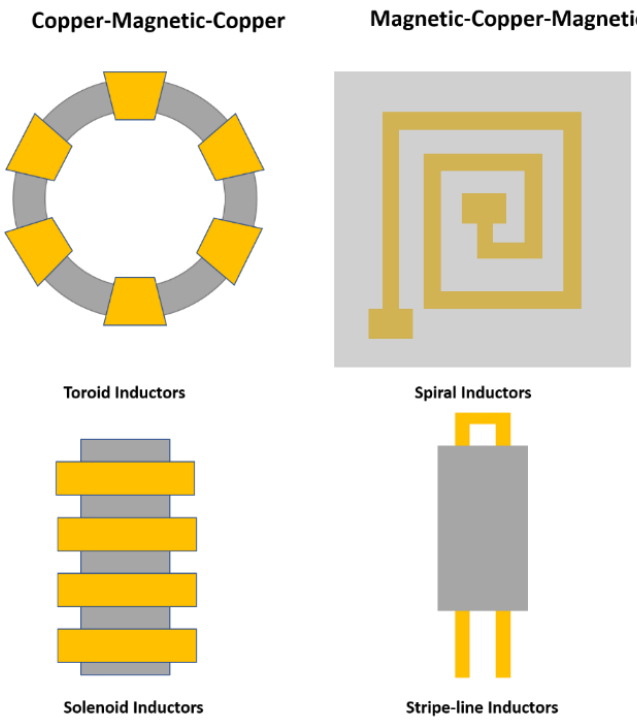

Figure 2.12: Various magnetic-core inductor structures

2.2.1 CMC (Copper-Magnetic-Copper) -based topologies:

Solenoid inductors belong to the CMC class of inductors. These inductors generate uniaxial magnetic field inside the winding loops and prevent unwanted electromagnetic (EM) interaction with other components. The solenoid inductors show high current handling when the uniaxial magnetic field is along the hard axis. This requires magnetic cores to have uniaxial anisotropy. This can be achieved easily by applying uniaxial external magnetic field during the deposition of magnetic cores [35].

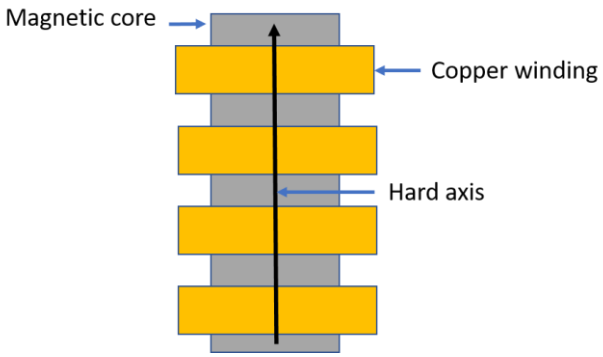

Figure 2.13: Solenoid inductors with magnetic field along the hard axis of the magnetic cores

Similar to solenoid inductors, toroidal inductor structure also constrains all the magnetic field within the winding loop. However, solenoid inductors are preferred because uniaxial anisotropy can be induced easily. The toroidal inductors require radial anisotropy as show in Figure 2.14. It is difficult to induce radial anisotropy in magnetic cores. Sullivan et al., [36] developed a set-up with concentric cylindrical magnetic bars to induce radial anisotropy into magnetic cores for high current handling as shown in Figure 2.15 [37].

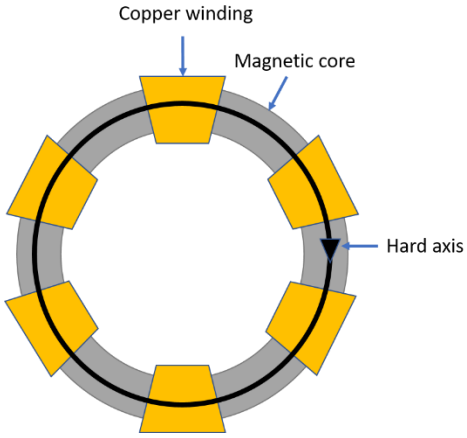

Figure 2.14: Toroidal inductors with radial anisotropy

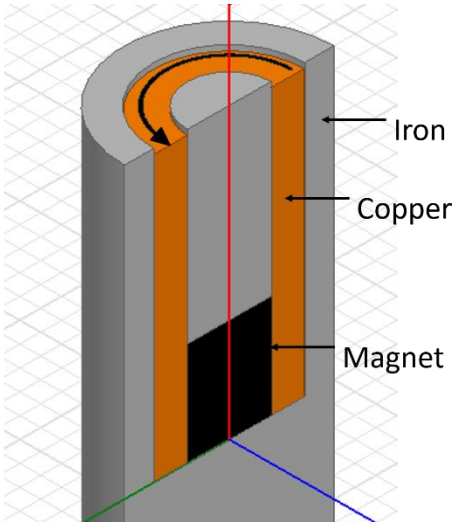

Figure 2.15: Structure used to induce radial anisotropy into magnetic cores

2.2.2 MCM (Magnetic-Copper-Magnetic) -based topologies:

Spiral inductors are planar structures and belong to the MCM category. The entire copper windings of spiral inductor are sandwiched with two magnetic layers, as shown in Figure 2.12. The inductance depends on the number of turns of copper windings. A large number of turns can lead to high inductance density for spiral inductors. Thick and wide copper traces will lower the DC resistance. This can be easily accomplished with 2D planar spiral copper structures. However, because the magnetic field of spiral inductors is oriented in all directions, the field cannot be aligned along the hard axis of magnetic cores alone, for high current handling. The randomly-oriented field requires the magnetic cores to be isotropic, which lowers the current handling.

To fully utilize the planar inductor in power applications, the magnetic-core shape needs to be configured in a way that the magnetic field can be aligned along the hard axis, as shown in Figure 2.16. This structure is called a “racetrack inductor”. The copper windings are elongated longitudinally to enhance the transverse magnetic field strength.

With the field dominating the transverse direction, the magnetic core can be engineered to have hard axis along the same direction and result in high current-handling. However, the field also has to go through the thickness of the magnetic films. This is a concern because of the low permeability and high coercivity in the out-of-plane direction with thin magnetic films.

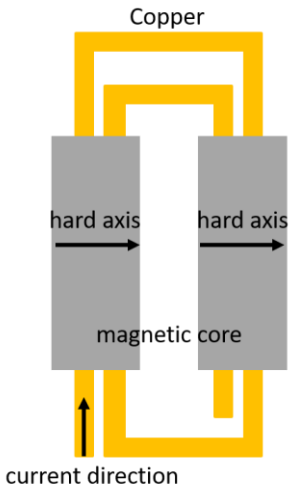

Figure 2.16: Racetrack inductor with magnetic field along the hard axis of the magnetic core.

The current handling of planar inductors can be further improved with reduction in the number of turns. Planar inductors, as shown in Figure 2.17, with one turn are called stripline inductors and shows high current-handling because of weak magnetic fields. In addition to the high current handling, the stripline inductors also have high inductance density because of the small size.

Table 3 summarizes the advantages and disadvantages of four major inductor structures. [38]

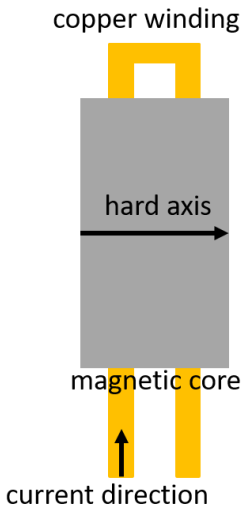

Figure 2.17: Strip-line inductor with magnetic field along the hard axis.

Table 3: Advantages and disadvantages of various inductor structures [38].

	Inductance density	Current handling	Process fabrication	Design complexity
Solenoid				
Toroid				
Spiral				
Stripe				

CHAPTER 3. MAGNETIC MATERIAL DESIGN

Ideal magnetic materials for power inductors should have the following properties.

1) **High permeability**: High permeability is critical to realize the miniaturization of power inductors. Higher permeability leads to higher inductance and energy storage densities. In other words, for the same energy storage, inductors with high-permeability magnetic cores require small footprint.
2) **High-frequency stability**: Magnetic materials show high permeability at low frequency. The permeability decreases with increasing in frequency. For inductors to work at high-frequency range, magnetic materials are expected to have stable and high permeability at those operation frequencies.
3) **Scalability**: Thick magnetic cores are desired because of low reluctance. For the same inductor structures, thicker magnetic cores lead to lower reluctance and higher inductance. Thus, a higher L/R_{DC} value can be achieved without changing the structure and DC resistance of inductors.

This chapter discusses modeling and design of magnetic particles with high-permeability and high-frequency stability. Effect of particle shape and size on permeability and frequency stability are emphasized because this is the most dominant effect in magnetic particle composites. General design rules are generated to assist the design of magnetic particles. For scalability, metal-polymer composite approach is adopted. This approach allows magnetic materials to be scaled to thick component for low reluctance.

3.1 Shape Effect

It is known that permeability shows strong dependence on particle shape. For spherical particles, the permeability along all directions is the same, resulting in isotropic permeability. For disk particles, the permeability along out-of-plane direction is smaller

than in-plane direction, resulting in anisotropic permeability. This phenomenon arises from the demagnetization that arises from shape anisotropy.

Under external applied field, magnetic particles are magnetized to induce magnetic poles on the particle surface. These poles generate internal fields, referred to as demagnetizing fields, and oppose the external field as shown in Figure 3.1. Because of the opposing demagnetizing field, the effective field experienced by the particles is reduced, resulting in lower magnetization and permeability. The strength of the internal field depends on the distance between magnetic poles. For disk particles, the in-plane demagnetizing field is weaker than the out-of-plane field due to the longer distance. As a result of the weak demagnetization, the effective field along the in-plane direction is stronger than out-of-plane direction. Thus, the permeability is higher along in-plane direction than out-of-plane direction.

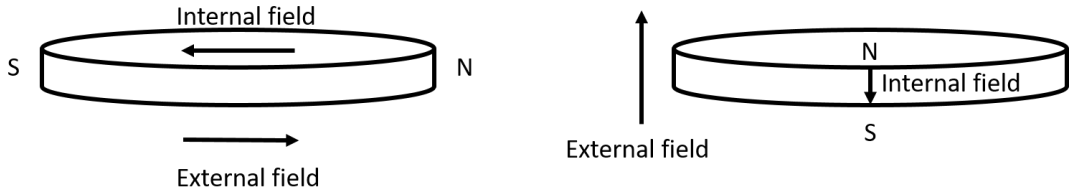

Figure 3.1. Magnetized particle with induced demagnetizing field

Since external field causes larger effective field along the in-plane direction, the ferromagnetic particles are easily saturated. Thus, in-plane direction is called easy axis and shows high permeability. Similarly, the out-of-plane direction is called hard axis since the particles experienced smaller effective field. Large external field is required to overcome the demagnetization and saturate the particles. Figure 3.2 shows the BH loops of easy axis and hard axis.

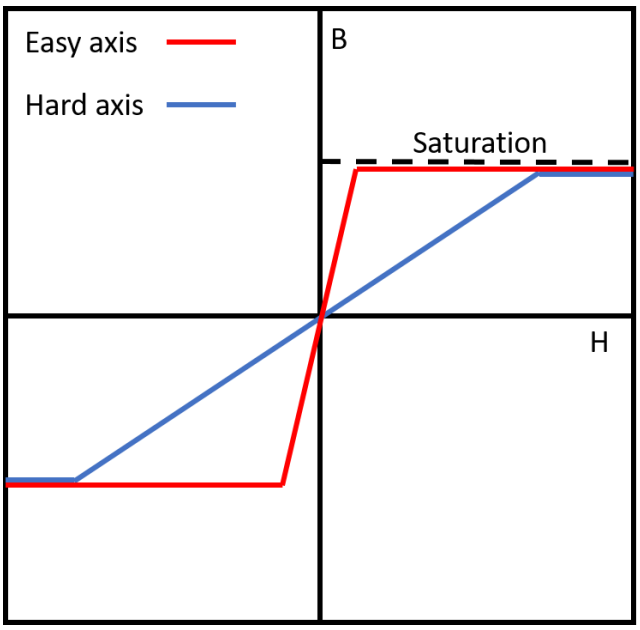

Figure 3.2: BH loop along easy axis and hard axis.

The effective field on the particles can be described as [39]

$$H_{eff} = H_{ext} - H_{demag} = H_{ext} - NM \tag{3.1}$$

where M is the magnetization, H_{ext} is the external applied field, H_{demag} is the internal induced demagnetizing field, N is the demagnetizing factor, which shows strong dependence on particle shape. Table 4 shows the demagnetizing factor for different particle shapes. In SI units, the sum of demagnetizing factors along three orthogonal directions equal to one as described by

$$N_x + N_y + N_z = 1 \tag{3.2}$$

Table 4: Demagnetizing factors for different particle shapes

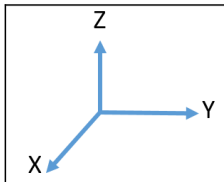	sphere 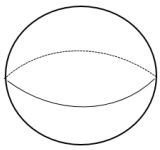	Infinite-long rod 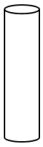	Infinite-long plane 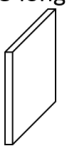
Nx	1/3	1/2	0
Ny	1/3	1/2	1
Nz	1/3	0	0

For spherical particles, the demagnetizing factor along three axes is equal, indicating absence of shape anisotropy. Therefore, the permeability of spherical particles is expected to be the same for all directions. Shape anisotropy is observed in rod and flake particles. For rod particles, zero demagnetizing factor along z-axis indicates the direction of easy axis. When the particles are magnetized under external applied field, the permeability is expected to be higher along z-axis as compared with x- and y-axis. For thinfilms, the easy-axis is within the flake plane. Thus, the in-plane permeability is expected to be higher than out-of-plane permeability.

By solving the Landau-Lifshitz-Gilbert (LLG) equation as stated below, permeability spectrum can be obtained.

$$\frac{dM}{dt} = -|\bar{\gamma}|MxH_{eff} - |\bar{\gamma}|\frac{\alpha}{M_s}M \times \left[M \times H_{eff}\right] \quad (3.3)$$

where M is the magnetization, H_{eff} is the effective field, $\bar{\gamma}$ is the Landau-Lifshitz gyromagnetic ratio, and α is the damping constant. The first term in this equation describes the precession motion of magnetization under external applied load while the second describes the damping motion of magnetization under external applied load. The damping motion leads the magnetization to align with the external applied field and reach the minimum energy state. Figure 3.3 illustrates the precession motion of magnetization with damping.

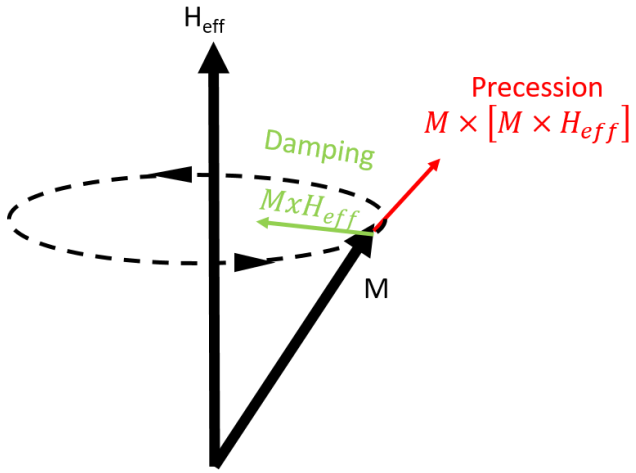

Figure 3.3: Precession motion of magnetization with damping

The solutions of LLG equation are given by [40]

$$\mu_x = \frac{\omega_m(\omega_0 + \omega_m N_y)}{\omega_0^2 - \omega^2 + \omega_0\omega_m(N_x + N_y) + \omega_m^2 N_x N_y} + 1 \tag{3.4}$$

$$\mu_y = \frac{\omega_m(\omega_0 + \omega_m N_x)}{\omega_0^2 - \omega^2 + \omega_0\omega_m(N_x + N_y) + \omega_m^2 N_x N_y} + 1 \tag{3.5}$$

where $\omega_0 = \mu_0\gamma(H_k - N_z M_s) + i\alpha\omega$, $\omega_m = \mu_0\gamma M_s$ and ω is the angular frequency of external field. The solutions assume that particles are saturated along z-axis. Thus, permeability along z-axis is 1. At low frequency ($\omega = 0$), the two equations can be simplified, as shown below, to study the effect of shape on permeability.

$$\mu_x = \frac{M_S}{H_K + M_S(N_X - N_Z)} + 1 \tag{3.6}$$

$$\mu_y = \frac{M_S}{H_K + M_S(N_y - N_Z)} + 1 \tag{3.7}$$

For Fe, with M_s and H_k of 1.8e6 A/m and 4.5e4 A/m [40], the calculated permeability along x-axis and y-axis is tabulated Table 5. It appears that spherical particles are preferred since the permeability is large along all directions. However, the calculated permeability is only good for low frequency ($\omega = 0$). To design the right shape, frequency stability needs also to be considered.

Table 5: Calculated permeability along x-axis and y-axis.

	sphere	Infinite-long rod	Infinite-long film
μ_x	40	3	40
μ_y	40	3	2

3.1.1 Ferromagnetic Resonance (FMR)

As mentioned before, both permeability and frequency stability need to be considered during modeling and design of magnetic particles. In addition to the permeability, particle shape also affects the frequency stability of magnetic materials [41].

As described in Figure 3.3, magnetization precesses around a static field. The frequency of precession depends on several things such as the shape of the particle, the strength of the field and the magnetization etc. If a microwave field with the same frequency as the precession frequency is applied perpendicular to the static field, a large amount of energy will be absorbed, resulting in local heating of the materials. This phenomenon is called ferromagnetic resonance (FMR) and the frequency is called FMR frequency. The magnetic materials need to be designed to have FMR frequency 3X larger than the operation frequency to avoid high energy loss.

For bulk materials, under no external applied field, the FMR frequency can be calculated as [42]

$$f_{FMR} = \mu_0 \frac{\gamma}{2\pi} H_k \tag{3.8}$$

where H_k refers to the net intrinsic field anisotropy. With shape anisotropy and external applied fields, the equation is modified and described as [41]

$$f_{FMR} = \mu_0 \frac{\gamma}{2\pi} \left[(H + (N_y - N_z) M_s)(H + (N_x - N_z) M_s) \right]^{1/2} \tag{3.9}$$

Equation (3.9) assumes that the microwave field is applied along x-axis. The FMR frequency for common particle shapes is then calculated and tabulated in Table 6. H refers to the combination of intrinsic field anisotropy and applied magnetic field.

Table 6: FMR frequency of different particle shapes

Z Y X	sphere	Infinite-long rod	Infinite-long plane
Nx	1/3	1/2	0
Ny	1/3	1/2	1
Nz	1/3	0	0
f_{FMR}	$f = \mu_0 \frac{\gamma}{2\pi} H$	$f = \mu_0 \frac{\gamma}{2\pi} (H + \frac{1}{2} M_s)$	$f = \mu_0 \frac{\gamma}{2\pi} (H(H + M_s))^{\frac{1}{2}}$

It can be seen that by changing the shape from sphere to rod or disk, FMR frequency is increased. Magnetic materials can then be used for higher-frequency applications. For Fe material, the calculated FMR is tabulated in Table 7 together with x-axis permeability. Table 7 indicates that particles with thin-film shape are preferred due to their combination of good permeability and frequency stability.

Table 7: Calculated x-axis FMR and permeability for different particle shapes.

	sphere	Infinite-long rod	Infinite-long film
μ_x	40	3	40
FMR	1.6 GHz	32 GHz	10 GHz

3.2 Size Effect

3.2.1 Eddy-Current Loss

Based on the previous analysis, particles with thin-film shape are preferred due to the combination of good permeability and frequency stability. However, this frequency stability only includes the FMR effect. For conductive magnetic particles, eddy-currents also play an important role in determining the frequency stability of magnetic particles. To design the right particle size, eddy current loss needs to be discussed.

According to Faraday's law, a changing magnetic field induces circular electric current within conductors, which leads to energy loss in term of heat in non-zero resistivity materials. This loss is known as eddy current loss. This loss is proportional to the size, resistivity and operation frequency as stated in [27, 43]

$$\mu'' = \frac{2\pi(\mu')^2\sigma d^2 f}{3} \tag{3.10}$$

where σ is the conductivity, d is the particle size and f is the operation frequency. Since high-permeability metal particles are chosen as the candidates for magnetic cores, there are no modifications for the conductivity. Thus, the only way to lower the eddy current loss is to use smaller particles. The frequency above which the eddy current loss is dominant can be estimated using Equation (3.11) [27].

$$F_{EC} = \frac{4\rho}{\pi\mu_r\mu_0 D^2} \tag{3.11}$$

where ρ and D are particle resistivity and diameter respectively. As a combination of good core loss, DC bias stability and high-temperature stability, Sendust ($Fe_{85}Si_9Al_6$) particles are chosen for this research. For spherical Sendust particles with resistivity of 106 μΩ*cm,

the estimated frequencies above which the eddy current loss is dominant for various particle sizes are plotted in Figure 3.4 [44]. The plot indicates that particles with diameter smaller than 30 μm should be used for the target frequency of 10 MHz.

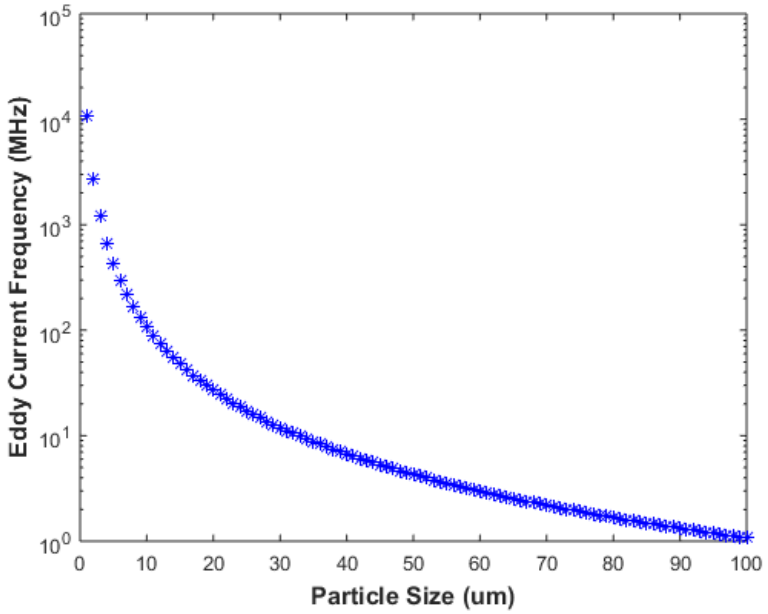

Figure 3.4: Various sendust particle sizes and the corresponding frequencies above which eddy current loss is dominant.

Although Equation (3.11) is used for spherical particles, the predicted number can also be used as a conservative estimate for particles with thin-film shape. Figure 3.5 shows two spherical particles with the same diameter. One particle system consists of homogenous magnetic material. The other system consists of magnetic thin-films separated by alternating insulation films. Because of the insulation film, eddy currents are unable to circulate on wide arcs, resulting in low eddy current loss. Therefore, the estimated number from Equation (3.11) can be used as a conservative number for particles with flake or thin-film shape.

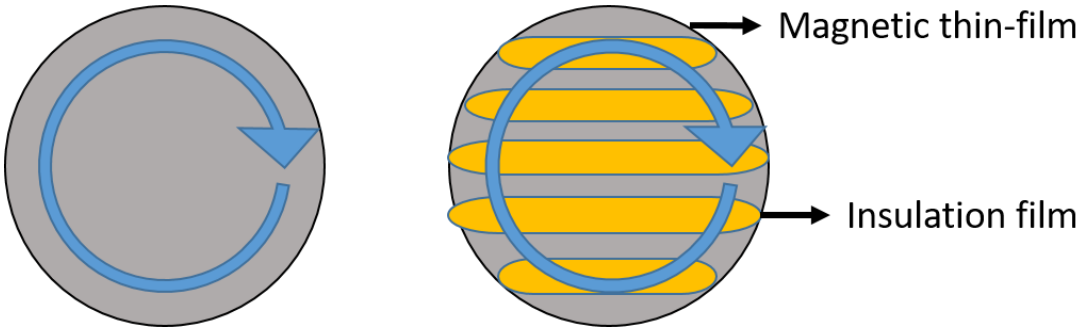

Figure 3.5: Illustration of circulation of eddy current in two particles.

Based on vendor's availability, Sendust flakes with average in-plane diameter of ~40 μm and thickness of ~1 μm are chosen as the magnetic cores for inductors. The flakes have thin-film shape for a good combination of permeability and frequency stability. The size is chosen so that the flakes can work at 10 MHz without significant eddy current loss. The saturation magnetization (M_s) and anisotropic field (H_k) of flakes are measured with vibrating sample magnetometer. The $\mu_0 * M_s$ and H_k of the flakes are 1 T and 2000 A/m respectively. According to Equation (3.6), the predicted low-frequency permeability is around 399 for the Sendust flakes.

3.3 Scalability

Sendust flakes are mixed with epoxy resin to make metal-polymer magnetic composites for inductors. There are three advantages of mixing Sendust flakes with epoxy resin. First advantage is the scalability. The composite can be scaled up easily to form thick magnetic cores for inductors. The thick magnetic cores give high L/R_{DC} value to inductors, as mentioned at the beginning. Second advantage is the high resistivity. The flakes are coated with an insulating resin to avoid electrical contact, which can lead to high eddy current loss. The third advantage is process capability. The composites can be synthesized

as flexible sheets, as shown in Figure 3.6. The flexibility allows the composites to be processed as regular dielectric dry-films that are widely used in electronic packages. Therefore, the magnetic composites can be easily integrated into electronic packages without introducing major process challenges.

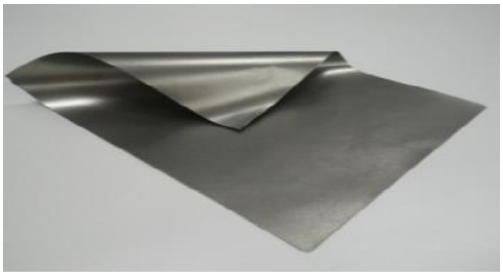

Figure 3.6: Photo image of flexible metal-polymer composite in the form of sheet (Courtesy to Nitto Denko)

Based on the vendor's process capability, the flakes are mixed with epoxy resin with a volume ratio of 60% flakes and 40% epoxy resin. Proprietary process is used to align all the flakes along one direction as shown in Figure 3.7. The alignment gives high-permeability along one direction for the polymer-flake composites.

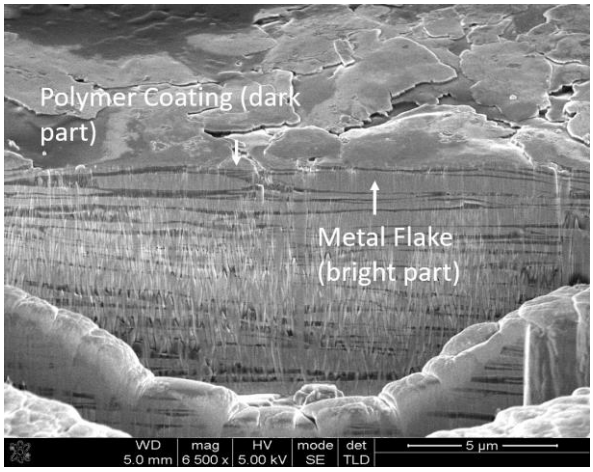

Figure 3.7: Cross-section of metal-polymer composite

Bruggeman's effect medium theory, as stated in Equation (3.12), is used to predict the permeability of the flake-polymer composites [39, 40].

$$c_f \frac{\mu_f - \mu_c}{\mu_f + 2\mu_c} + c_p \frac{\mu_p - \mu_c}{\mu_p + 2\mu_c} = 0 \tag{3.12}$$

where c_f and c_p are the volume fraction of flake and polymer respectively. μ_f, μ_p and μ_c are the permeabiliy of flake, polymer and composite resectively. The permebaility of polymer is assumed to be 1 in this case. With $\mu_f = 399$, $c_f = 60\%$ and $c_p = 40\%$, the composite is estimated to have low-freqeuncy permeability of 161, according to Equation (3.12).

The complex permeability spectrum of the metal-polymer composite is measured using a vector network analyzter (VNA). The results are shown in Figure 3.8. The real permeability is shown in back line while the imaginary permeability is shown in red line.

The composites show a stable permeability of 141 till 10 MHz. The predicted values are slight higher than the measured values, indicating that the analytical equations can be used a general gulideline for the design of magnetic composites. This composite is then used as the magnetic core of power inductors.

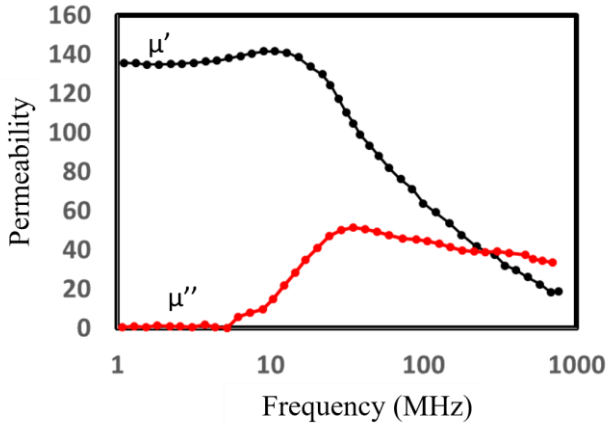

Figure 3.8: Complex permeability spectrum of flake-polymer composite (Courtesy to Nitto Denko).

3.4 Chapter Summary

Modeling and design of magnetic particles are discussed in this chapter. Three major particle shapes, sphere, rod and film, are emphasized. Particles with film-like shape are preferred because of the good combination of high-permeability and high-frequency stability. Based on the design guidelines, Sendust flakes with in-plane diameter of ~40 μm and thickness of 1 μm are selected and mixed with epoxy resin, with a volume ratio of 60% to 40%, to synthesize the magnetic composites. The composites can be scaled up easily to handle high current. Electric characterization shows that the magnetic composites have stable permeability of 141 till 10 MHz, as predicted by the design guides.

CHAPTER 4. INDUCTOR DESIGN

This chapter describes inductor design with advanced metal-polymer composites. The first part of this chapter presents the concept of magnetic circuits used for inductor designs. Two important parameters, inductance and current handling, are calculated using the magnetic circuits. Losses from inductor windings are discussed in the second part. Based on the loss analysis, design rules for inductor windings are also concluded in the second part. In the last part, several inductor structures such as 2D spiral or 3D solenoid topologies are modeled and designed to achieve the objectives defined in Chapter 1. Finite element method (FEM) is used during the design process to get more accurate results as compared to magnetic circuits.

4.1 Magnetic Circuit Concept

Inductors are important energy storage components in voltage converters. Their main function is to supply stable voltage at the loads. A voltage converter based on buck switching regulator is shown in Figure 4.1.

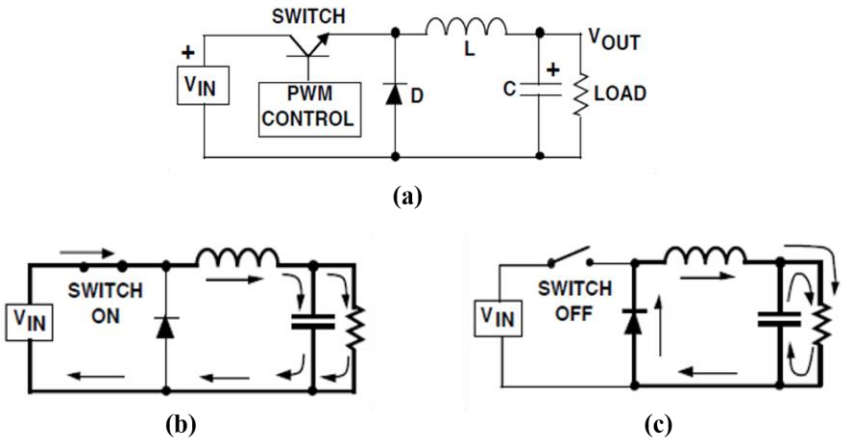

Figure 4.1: (a) Electric circuit of a switching voltage regulator, (b) On-state and (c) Off-state of a switching voltage regulator. [45]

When the switch is on as shown in Figure 4.1 (b), electric current goes through the inductor and energy is stored in the magnetic field of the inductor. When the switch is off, the stored energy is then released from the magnetic field and used to support voltage to the loads. The amount of energy stored in inductor is defined as

$$E = \frac{1}{2} L i^2 \tag{4.1}$$

where i is the current passing though the inductor. L is inductance of the inductor which is defined as

$$L = \frac{N * \Phi}{i} \tag{4.2}$$

where N is the number of winding turns of inductor and Φ is the generated magnetic flux from inductor. According to Amp's law, the magnetic flux has a strong dependence on the length of inductor, number of inductor windings and inductor cross-sectional area. Therefore, by designing the inductor structure, the desired inductance can be achieved.

Inductors with magnetic materials can be presented as components in a magnetic circuit, similar to resistors and voltage sources in an electric circuit. With this concept, the inductance can be solved using similar methods developed for electric circuits. Table 8 and Figure 4.2 below show the similarity between a magnetic circuit and an electric circuit [46].

Table 8: Comparison between the concept of electric circuit and magnetic circuit

Electric circuit	Symbol	Magnetic circuit	Symbol
Electromotive force (EMF)	$\varepsilon = v = \int Edl$	Magnetomotive force (MMF)	$F = Ni = \int Hdl$
Current	I	Magnetic flux	Φ
Current density	$J = \frac{I}{A}$	Magnetic flux density	$B = \frac{\Phi}{A}$
Conductivity	σ	Permeability	μ
Resistance	$R = \frac{l}{\sigma A}$	Reluctance	$\mathcal{R} = \frac{l_m}{\mu A}$

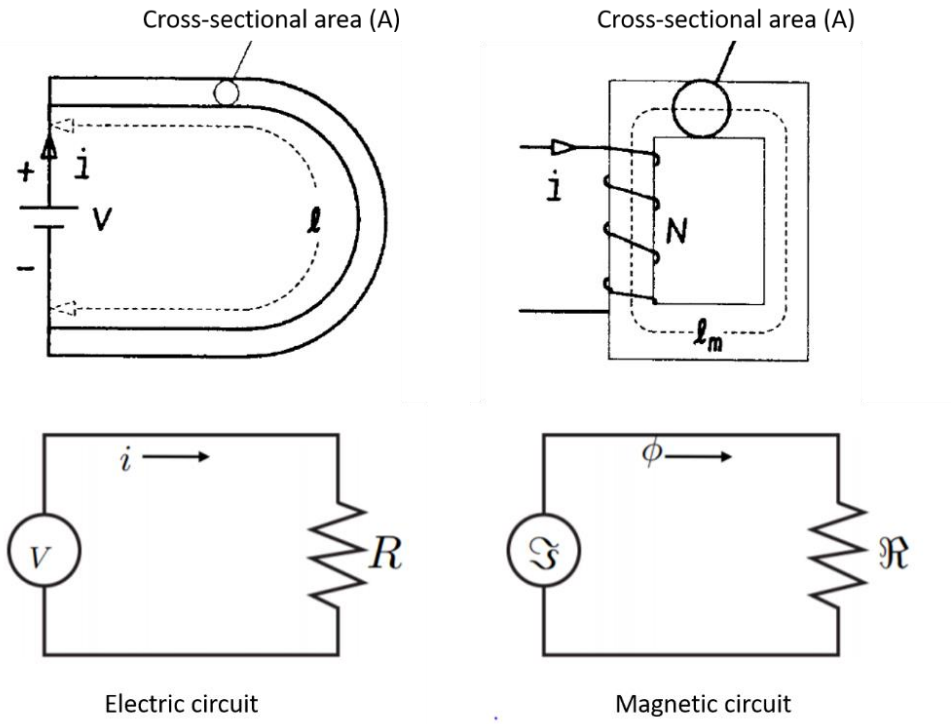

Figure 4.2 Similarity between magnetic and electric circuits. [46, 47]

In electric circuit, the current in conductor can be calculated using Ohm's law

$$i = \frac{v}{R} \tag{4.3}$$

Similar to the electric circuit, the magnetic flux can be calculated using

$$\Phi = \frac{Ni}{\mathcal{R}} \tag{4.4}$$

Equation (4.4) indicates that the magnetic flux increases with increasing inductor current. At a high current value, increasing in current will not lead to a further increase in magnetic flux because of the saturation of magnetic cores. The saturation current, which is

an important parameter of power inductor, is derived as in Equation (4.5), where B_{sat} is the saturation magnetization of magnetic cores.

$$i_{sat} = \frac{\Phi\mathcal{R}}{N} = \frac{B_{sat}A\mathcal{R}}{N} \tag{4.5}$$

The saturation current is usually limited by the availability of high B_{sat} magnetic cores and footprint for inductors. The easiest way to increase saturation current is to increase the reluctance by introducing air gap, as shown in Figure 4.3.

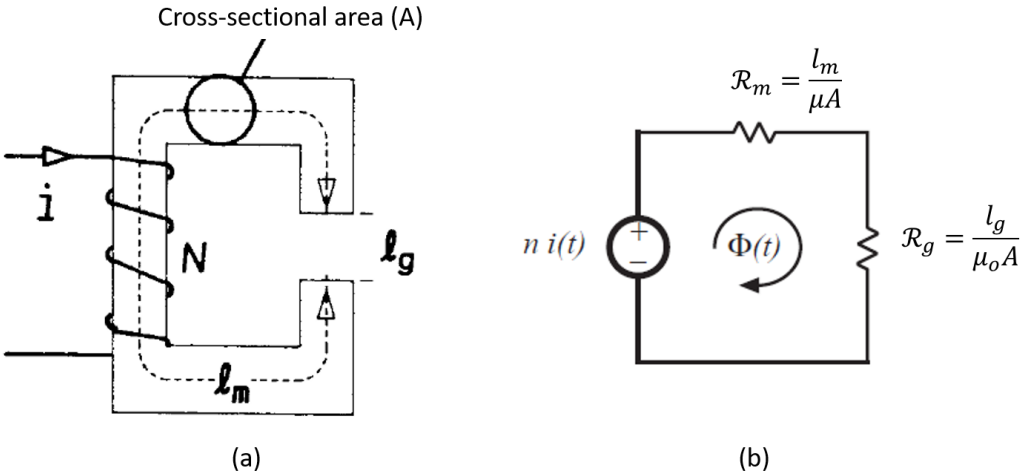

Figure 4.3: Magnetic-core inductor with introduced air gap to handle high current [46, 47]

In comparison to magnetic cores with high permeability of hundreds, air gap with permeability of one significantly increases the total reluctance, and therefore, the saturation current. For the magnetic core in Figure 4.3, the saturation current is calculated as

$$i_{sat} = \frac{\Phi\mathcal{R}}{N} = \frac{B_{sat}A(\mathcal{R}_m + \mathcal{R}_g)}{N} \tag{4.6}$$

Unlike the saturation current, the air gap has negative impact on the inductance, which is another important parameter for power inductor. For the same magnetic core in Figure 4.3, the inductance is modified from Equation (4.2) as

$$L = \frac{N\Phi}{i} = \frac{N^2}{\mathcal{R}} = \frac{N^2}{(\mathcal{R}_m + \mathcal{R}_g)} \tag{4.7}$$

The magnetic core shown in Figure 4.3 is a simple geometry known as toroid core. For simple geometries, the equations mentioned above can be derived easily and used to calculate the saturation current and inductance during inductor design procedure. For more complex geometries, finite element models (FEM) need to be used to design inductors. This is discussed in Section 4.3.

4.2 Winding Losses

In addition to the magnetic core losses, inductor windings also contribute to the overall loss. At low frequency, the major contribution to the winding loss is DC loss. Figure

4.4 shows a typical current waveform of an inductor used in switching regulators under certain DC bias.

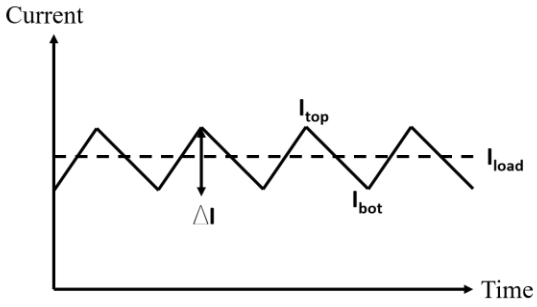

Figure 4.4: Typical current waveform of an inductor with rectangular voltage waveform

The ripple, load and mrs (mean root square) currents of this triangular current waveform are defined as [48]

$$I_{ripple} = \Delta I \tag{4.8}$$

$$I_{load} = \frac{I_{top} + I_{bot}}{2} \tag{4.9}$$

$$I_{rms} = \sqrt{I_{load}^2 + \frac{I_{ripple}^2}{12}} \tag{4.10}$$

With these definitions, the DC loss from inductor windings can then be calculated as [49]

$$P_{DC} = I_{DC}^2 R_{DC} \tag{4.11}$$

For small inductors, smaller wires are usually used. This leads to higher DC loss due to the smaller cross sectional area. For high-inductance inductors, larger number of windings is used, resulting in higher DC loss. The DC loss becomes extremely important for applications such as servers and graphics where tens or hundreds of current run thought

the conductors. During inductor design, thicker conductors, less number of windings and high-resistivity conductors need to be used whenever possible.

At higher frequency, another important term, AC loss, starts to contribute to the overall loss. The AC loss is calculated as Equation (4.12) where R_{AC} is the AC resistance of the inductor windings at a given frequency [49].

$$P_{AC} = I_{AC,rms}^2 R_{AC} = \frac{I_{ripple}^2}{12} R_{AC} \tag{4.12}$$

At higher frequency, the resistance increases because of skin effect. According to the Faraday's law of induction, a changing current within the conductor induces a changing flux perpendicular to the changing current. The changing flux, then, induces another type of currents, known as eddy currents, within the conductor. Based on Lenz's law, the eddy current loops have polarity opposite to the initial current. As a result, current is pushed to the surface of the conductor, leading to high current density at surfaces and low current density in the center, as illustrated in Figure 4.5. Therefore, the resistance increases since more current flows through a smaller area. Figure 4.6 shows the current distribution inside two circular copper wires at 1 GHz and at 10 GHz respectively. The wires have radius of 2 μm, with 10 A current running through them. At 1 GHz, current is uniformly distributed

across the whole cross section, leading to low AC resistance. At 10 GHz, more current is pushed towards the surface due to skin effect, leading to high AC resistance.

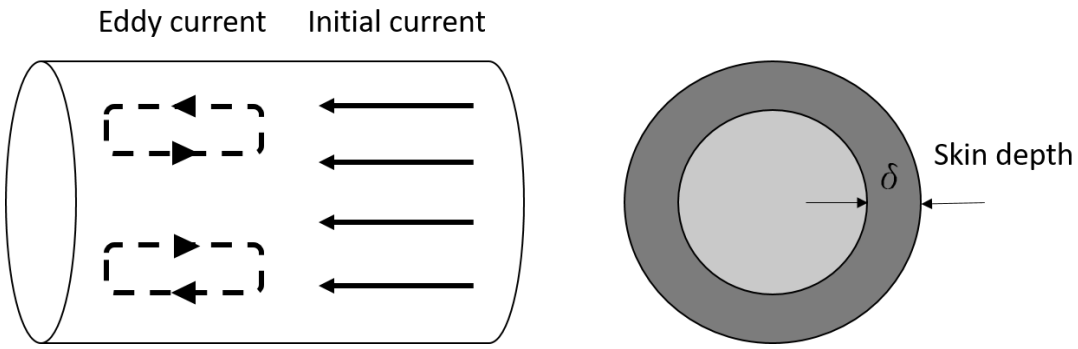

Figure 4.5: Illustration of skin effect in a circular conductor

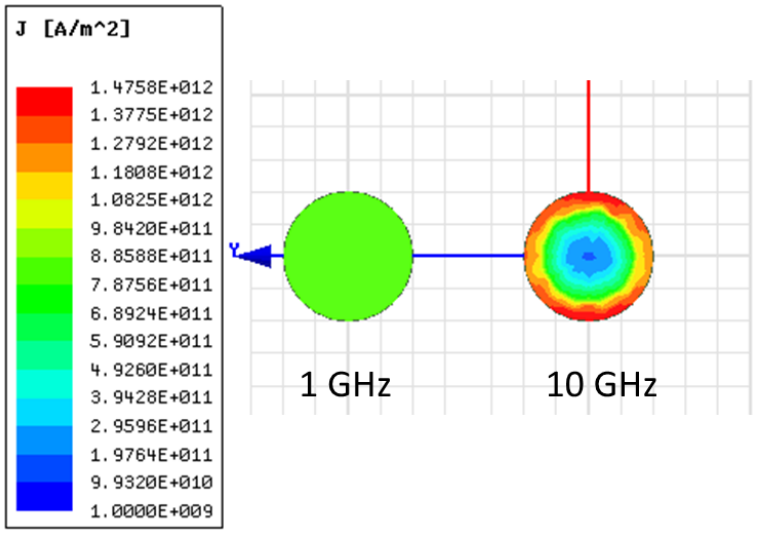

Figure 4.6: Illustration of skin effect inside conductors

The AC resistance can be calculated if the skin depth is given. The skin depth is defined as the depth where current drops to 1/e of the current at the surface (or at DC). This

depth depends on frequency (f), resistivity (ρ) and permeability (μ) of the conductor as stated below [49]

$$\delta = \sqrt{\frac{\rho}{\pi \mu f}} \tag{4.13}$$

Since the resistivity does not change, the ratio of R_{AC} to R_{DC} is simply the ratio of the area of the ring with a width equal to the skin depth to the area of the entire cross-section. The AC resistance of a circular conductor with radius of r is then calculated as [49]

$$\frac{R_{AC}}{R_{DC}} = \frac{\pi r^2}{\pi r^2 - \pi (r - \delta)^2} \tag{4.14}$$

To reduce the AC loss, flat conductor is preferred since it has more surface area as compared to circular conductor assuming both have the same cross-sectional area [50]. The more surface area leads to smaller AC resistance and lower AC loss. Figure 4.7 shows the AC loss of two copper wires with the same cross-sectional area but different shape. The

flat wire has more surface area, resulting in less AC loss, as compared to circular wires at all frequencies. During inductor design, flat wires will be used for all inductor structures.

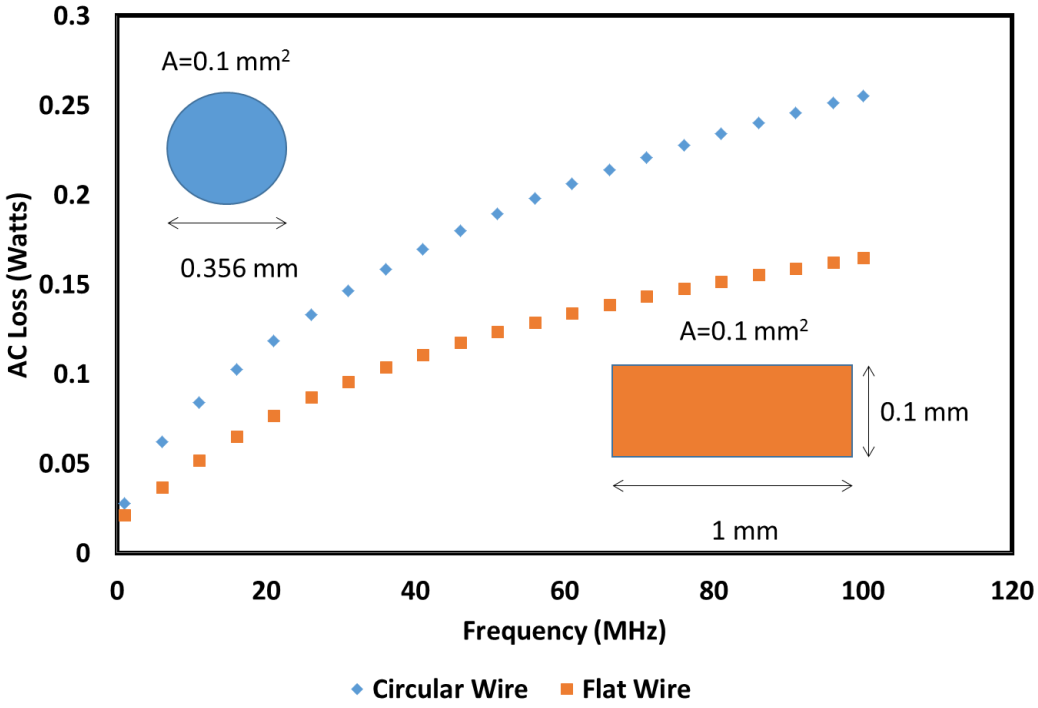

Figure 4.7: AC loss of two copper wires with the same cross-section area but different shape.

The AC resistance is further increased when multiple windings are placed near each other. This phenomenon is call proximity effect. When two wires are placed in together, the eddy current effect is enhanced. As the result, the current within the conductors are pushed to a smaller area instead of the entire area that is defined by the skin depth.

Therefore, the AC resistance is higher than the resistance caused only by the skin effect. Figure 4.8 illustrates proximity effect on the conducting area [50].

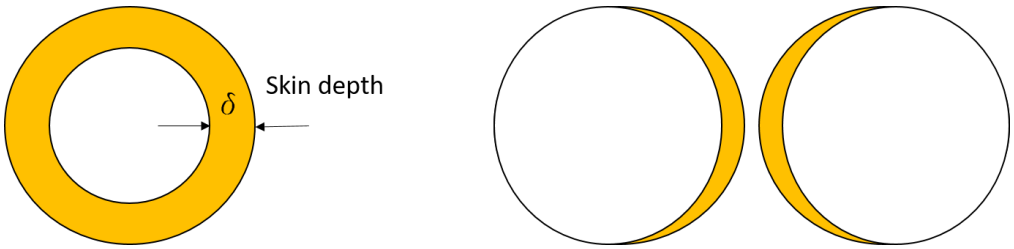

Figure 4.8: Illustration of proximity effect of the conducting area.

According to Dowell's method, the AC resistance under proximity effect shows strong dependence on the skin depth (δ), winding height (h) and number of winding layer (N) as stated below [51],

$$\frac{R_{AC}}{R_{DC}} \propto \delta, h, N \tag{4.15}$$

As the number of winding layer increases, the AC resistance increases dramatically. When combined with high AC current, the large AC resistance can lead to tremendous AC loss. For transformers, the multi-layer needs to be avoided since the ac component is stronger than dc component. For inductors, the ac component is usually a fraction (~10%) of dc component. Even though the ac resistance is high, the overall all ac loss can be small. Thus, inductors can be designed with multi-layer despite the proximity effect [51]. In this research, therefore, proximity effects are not considered during inductor design.

4.3 Inductor Design with FEM

As discussed in section 4.1, analytical equations are good for simple magnetic-core geometries such as toroids. For more complex geometries and more accurate results, finite

element method (FEM) is needed. ANSYS Maxwell, an electrical-magnetic (EM) simulation software, is used to design inductors in this research.

In the ANSYS Maxwell, the permeability spectrum and the hysteresis loop of magnetic cores are required to simulate the frequency-response and current-response of power inductors respectively. Various inductor structures are designed to achieve the specifications list in the Introduction. Table 9 re-captures the objectives.

Table 9: Inductor Objectives

Objectives	Unit	Objectives
1. High current handling	A/mm^2	1-2
2.High efficiency	nH/mΩ	10 - 20
3. Miniaturization	thickness (microns)	500

4.3.1 2D Spiral Inductors

2D spiral inductors were designed to achieve the objectives. Figure 4.9 shows the detailed dimensions of one designed inductors. This inductor has inductance of ~100 nH and DC resistance of 10 mΩ, leading to an efficiency of 10 nH/mΩ. The total thickness and size of the inductor is ~500 μm and ~ 10 mm^2. The copper windings are sandwiched between two magnetic sheets to form a closed magnetic loop, without any air-gaps, for high inductance with low DC resistance. However, simulation results show that this structure has low current-handling capability as shown in Figure 4.10. At 10 A DC current, the inductor shows 60% inductance drop. To be used at 10 – 20 A current range, power inductors need to show less than 30% inductance drop when comparing to the inductance

at 0 A. For 30% inductance drop, the design spiral inductor is estimated to have 3 A current handling.

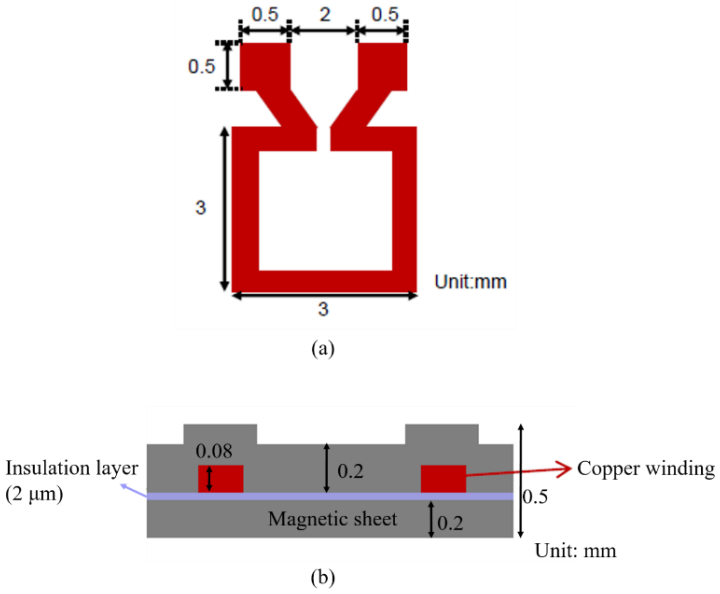

Figure 4.9: Dimensional details of the (a) Top-view and (b) Cross-section of the designed spiral inductors (Courtesy to Nitto Denko).

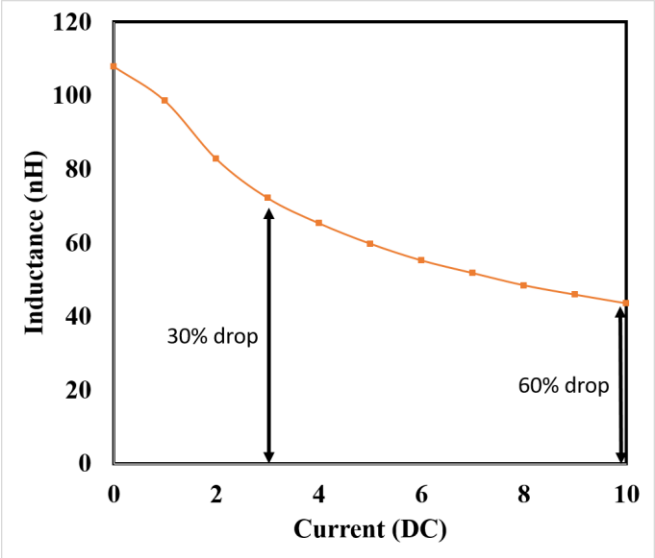

Figure 4.10: Simulated inductance of the optimized spiral inductor under an external applied DC current.

Without the need for new magnetic cores and new inductor designs, introduction of air-gap around the copper winding is the simplest way to increase the current handling capability. As illustrated in Figure 4.11, the current handling is increased because of the additional insulation layer. The insulation layer with permeability of one acts as the air-gap to increase the overall reluctance. According to Equation (4.6), high reluctance leads to high current handling capability. On the other hand, the insulation also results in low inductance and large thickness.

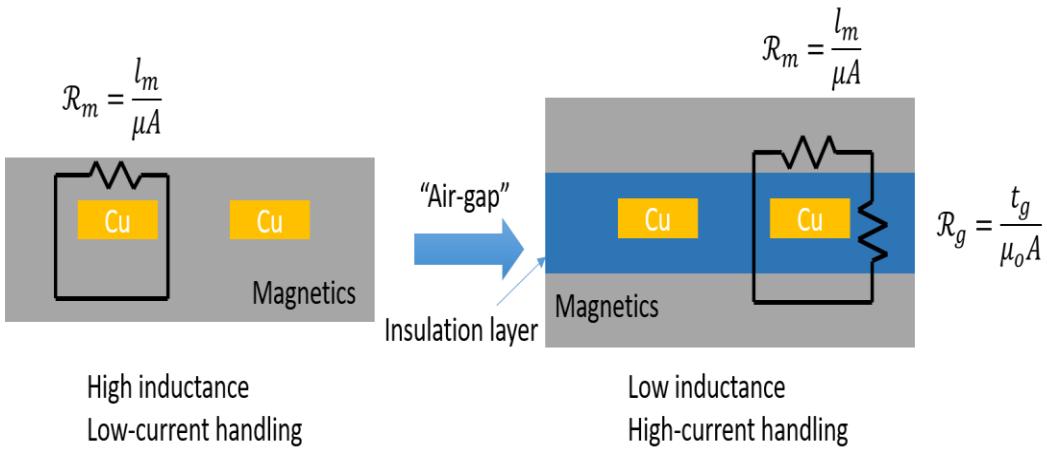

Figure 4.11: Schematic showing improvement of current handling by introducing "air-gap" around copper windings.

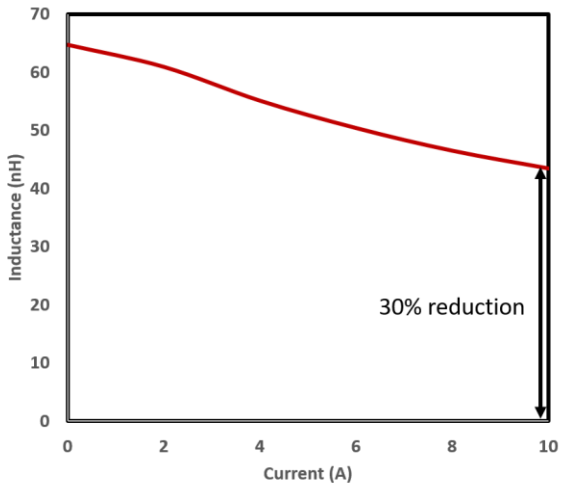

Figure 4.12: Simulated L vs I plot for the same inductors with air-gaps.

Figure 4.12 shows the simulated inductance of the same spiral inductor after introducing the 100 μm air-gap. With the "air-gap", the same spiral inductor shows 30% inductance drop at 10 A, meaning that the inductor can handle 10A current. However, the improvement in current handling comes at a price of reduced inductance.

4.3.2 3D Solenoid Inductor

Solenoid inductors with high-current handling capability are modeled and designed to achieve the target current-handling value [52]. The optimal design has inductance of 100 nH with a DC resistance of 11 mΩ, resulting an efficiency close to 10 nH/mΩ. The solenoid

inductor has an area of ~10 mm^2 and a thickness of ~600 μm. Dimension details of the solenoid inductors are shown in Figure 4.13.

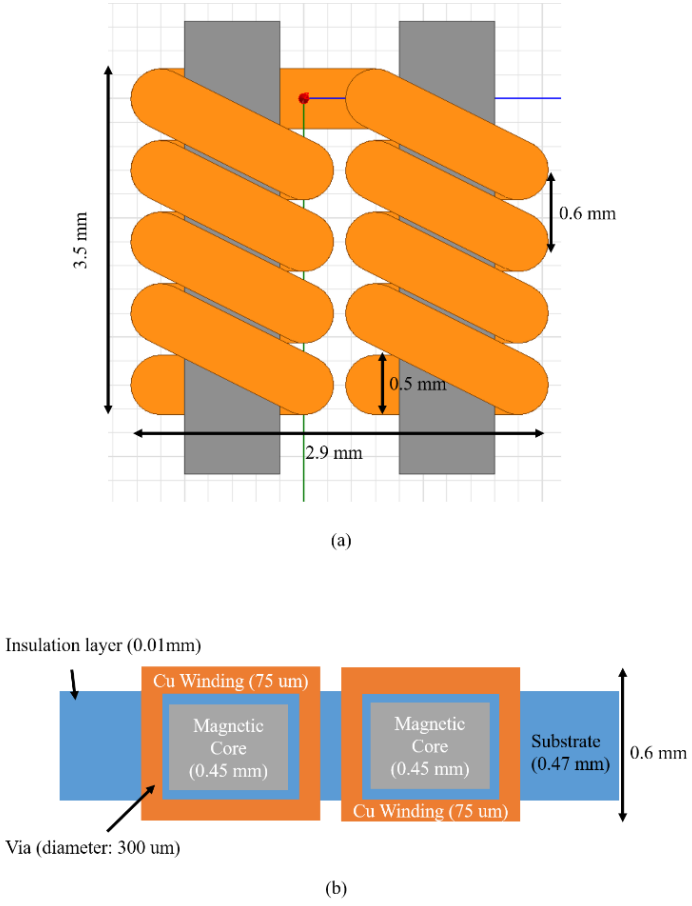

Figure 4.13: Dimension details of the (a) Top-view and (b) Cross-section of the designed solenoid inductors

Figure 4.14 shows the inductance density of the designed solenoid inductor under an externally-applied DC current. The designed solenoid inductor shows significant improvement in current-handling capability as compared to the spiral inductor. For the solenoid inductors, the current handling is estimated to be 12A. As compared to the 3A

current handling of spiral inductors, the solenoid inductors show 4x improvement in current handing.

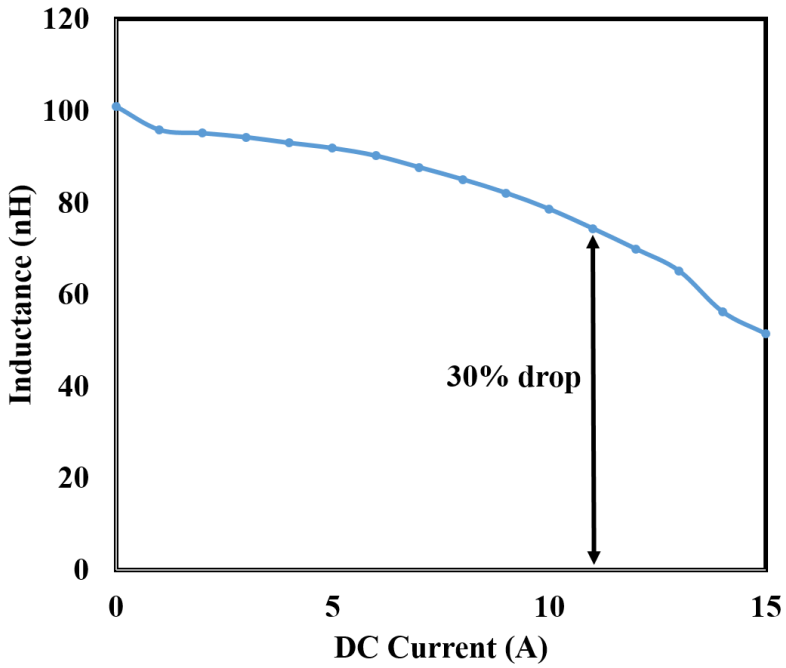

Figure 4.14: Simulated inductance of the solenoid inductor under external applied DC current.

4.4 Chapter Summary

The concept of magnetic circuit is presented to generate inductor design guidelines. For example, more number of winding turns can increase inductance at the cost of high DC loss. Introduction of an air-gap can improve the current handling at the cost of inductance. To get accurate results, finite element method (FEM) need to be used during inductor design process.

Various inductor winding losses are also presented in this chapter. They are DC loss, AC loss, loss from skin effect and loss from proximity effect. Based on the loss analysis, inductor with flat winding is used during design for low winding loss.

By using FEM, various inductor structures are modeled and designed to achieve the objectives. The simulated results show that inductors with spiral structure cannot achieve all the objectives simultaneously. By introducing air-gaps to the spiral inductors, current handling can be improved with a cost of inductance. Inductors with solenoid structure show better performance than spiral structure. Solenoid inductors are designed to achieve 12 A current handling with an L/R_{DC} value of ~ 10 nH/mΩ. The designed inductors have size of 10 mm^2 and thickness of ~ 600 μm.

CHAPTER 5. INDUCTOR FABRICATION AND CHARACTERIZATION

This chapter describes the fabrication and characterization of planar and 3D inductors. In order to realize the inductor designs from Chapter 4, novel processes are developed to fabricate and integrate the inductors into substrates. Details of the fabrication processes are also presented. The electrical characterization of the fabricated inductors is performed to demonstrate the advantages of using metal-polymer composites. The measured performance results of fabricated inductors are compared to the simulated results to demonstrate the performance improvements with the proposed designs and materials, and also validate the accuracy of FEM models.

5.1 Copper Winding Formation Processes

The microfabrication processes to form copper windings are briefly introduced this section. These processes are applied to the spiral and solenoid inductors in the subsequent sections.

5.1.1 Planar inductor processes

Planar inductors such as those based on spiral structures benefit from wide copper traces that lead to low DC resistance. Since the width is much larger than the thickness, subtractive patterning is widely used for these because of its process simplicity and low cost. The process flow is shown in Figure 5.1. A thick copper sheet is first laminated onto the substrate. A photo-sensitive polymer, known as photoresist, is then laminated onto the copper sheet to help with photolithographic patterning of copper. The photoresist is then

covered with photomask and exposed under UV light. The solubility of the photoresist changes with exposure, causing them to be selectively removed or retained. With negative photoresists that are used in this work, the unexposed part is then removed with solvent. By immersing the substrate into copper etchant, parts of copper sheet which are not covered with photoresist is etched away, resulting in inductor windings. The rest of photoresist is then removed with another solvent.

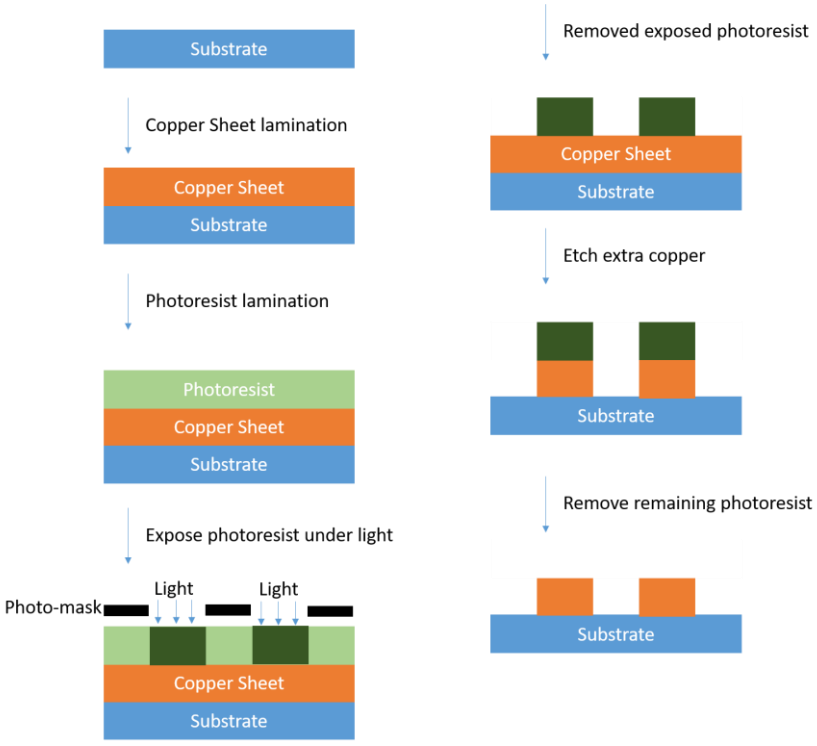

Figure 5.1: Process flow for 2D inductor fabrication

The subtractive etching process can easily form wide and thick copper windings in a short time. Such copper windings are desired for small DC resistance. One drawback about this process is the undercut, as shown in Figure 5.2. During the copper removal step, the copper etchant not only etches the copper traces vertically but also horizontally. This

causes the top of the trace to be narrower than the bottom. As a result, the measured DC resistance is lower than designed value since the cross-sectional area is smaller.

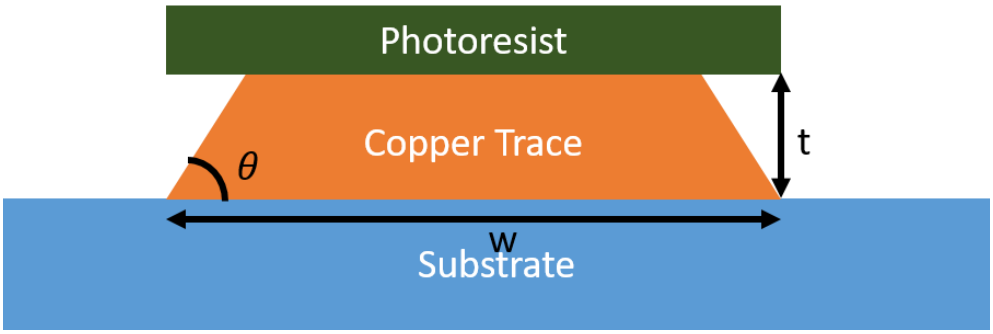

Figure 5.2: Cross-section of copper windings with undercut

The change in DC resistance between the designed value and measured value for copper traces with undercut can be estimated as

$$\Delta R_{DC} = \frac{wt}{wt - t * \frac{t}{\tan\theta}} - 1 \qquad \textbf{(5.1)}$$

where t is thickness of the copper trace, w is the width of the copper trace and θ is the angle between substrate and edge of the copper trance as illustrated in Figure 5.2. For the spiral inductor design presented in Chapter 3, the copper trances are designed to have thickness of 80 μm and width of 300 μm. The ΔR_{DC} of the inductor at various angles is plotted in Figure 5.3. For copper trace with severe under-cut effect ($\theta = 30^o$) [53], the changes in DC resistance can be as high as 85%. If the spiral inductors are designed to have 10 mΩ, the actual DC resistance will be 18.5 mΩ, resulting in a higher loss than the designed values.

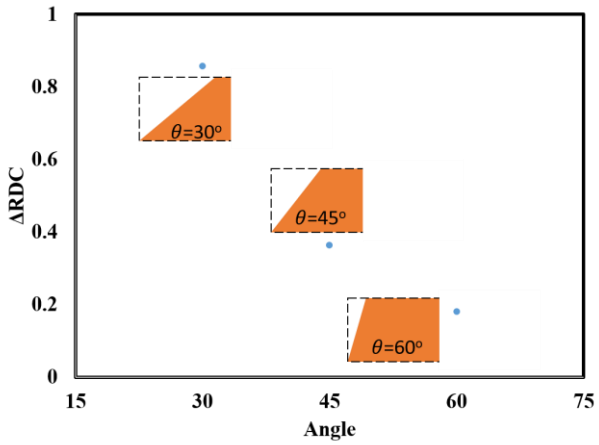

Figure 5.3: Changes in DC resistance after etching process

5.1.2 3D inductor fabrication process

In order to fabricate 3D copper windings with multilayered inductor structures such as those seen in solenoid inductors designs, an alternative process is used to fabricate copper windings. This approach is based on copper plating through photoresist micromolds with thin copper seed-layer. The copper seed-layer is etched away after removing the photoresist mold. The process is referred to as semi-additive patterning. This approach addresses the under-cut issue even with higher thickness/width ratios, as long as the seed-layer is much thinner than the feature sizes. It is a "from-bottom-up" process as opposed to the subtractive etching process. Figure 5.3 shows the process flow for the inductor fabrication. At the beginning, copper seed-layer with thickness of hundreds of nanometer is deposited onto the surface of the substrate using either physical vapor deposition (PVD) or electroless plating. A photoresist film is then laminated onto the seed-layer and exposed under photomask with UV light, and developed for photo-patterning. Copper windings are then plated through the photoresist by electroplating process. The thickness of the

photoresist determines the thickness of the copper windings. After electroplating, the photoresist and seed layer are then removed.

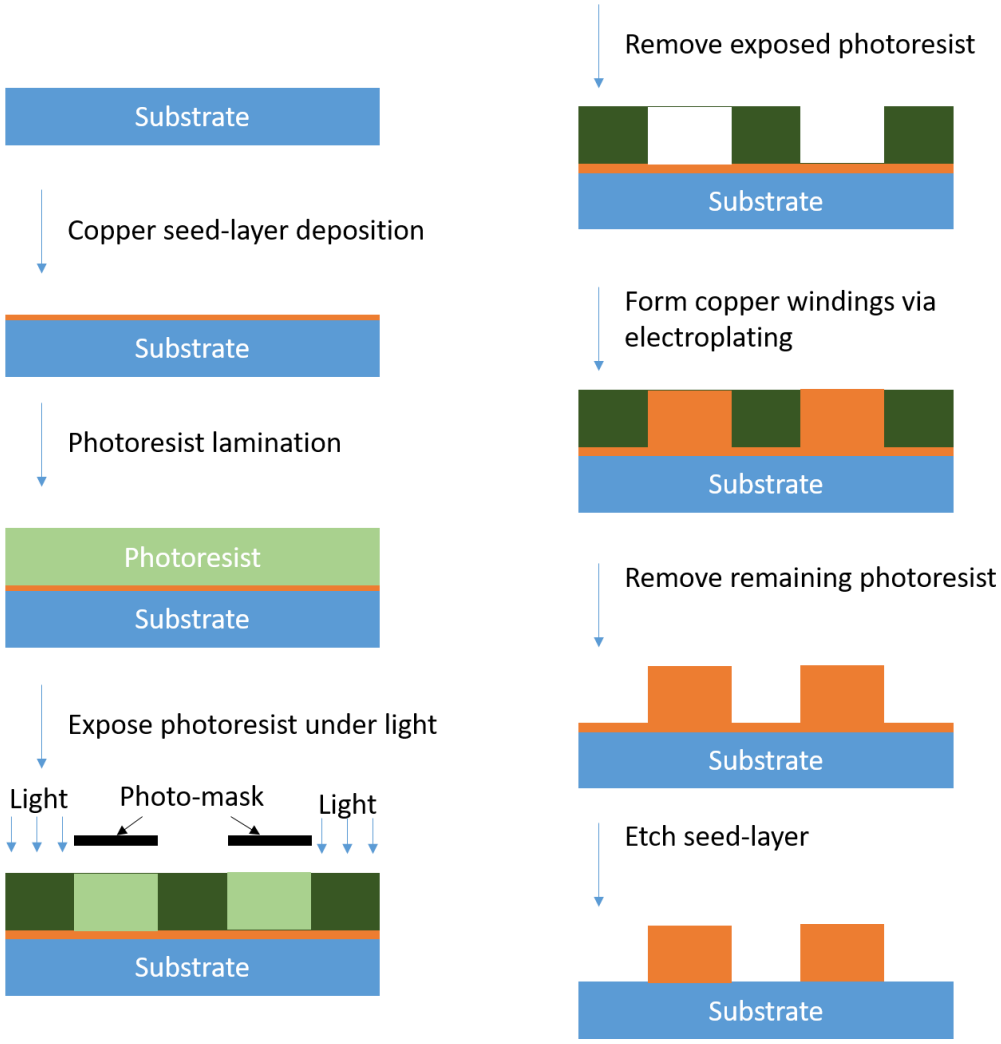

Figure 5.4: Process flow of semi-additive process

5.2 Core-less Spiral Inductors

For spiral inductors, copper windings were directly fabricated on 200 μm thick magnetic sheets to form a core-less structure without using organic substrates. The thick magnetic sheets were made strong enough to pass all substrate processes. The process flow

is shown in Figure 5.5. Ten-micron thick dielectric film was first laminated onto a 200μm thick magnetic film at 100 ºC and 0.3 MPa for 60s. The dielectric film was cured inside an oven at 180 ºC for 1 hour. Copper windings were then formed by subtractive etching process as mentioned before. Next, another 200μm thick magnetic films with laminated dielectric films were laminated onto the copper windings. At this stage, the copper windings were sandwiched between two magnetic films and a closed magnetic loop was formed for high inductance. UV laser was used to remove drill vias in the magnetic films to access the metallic surfaces of inductors for probing and testing.

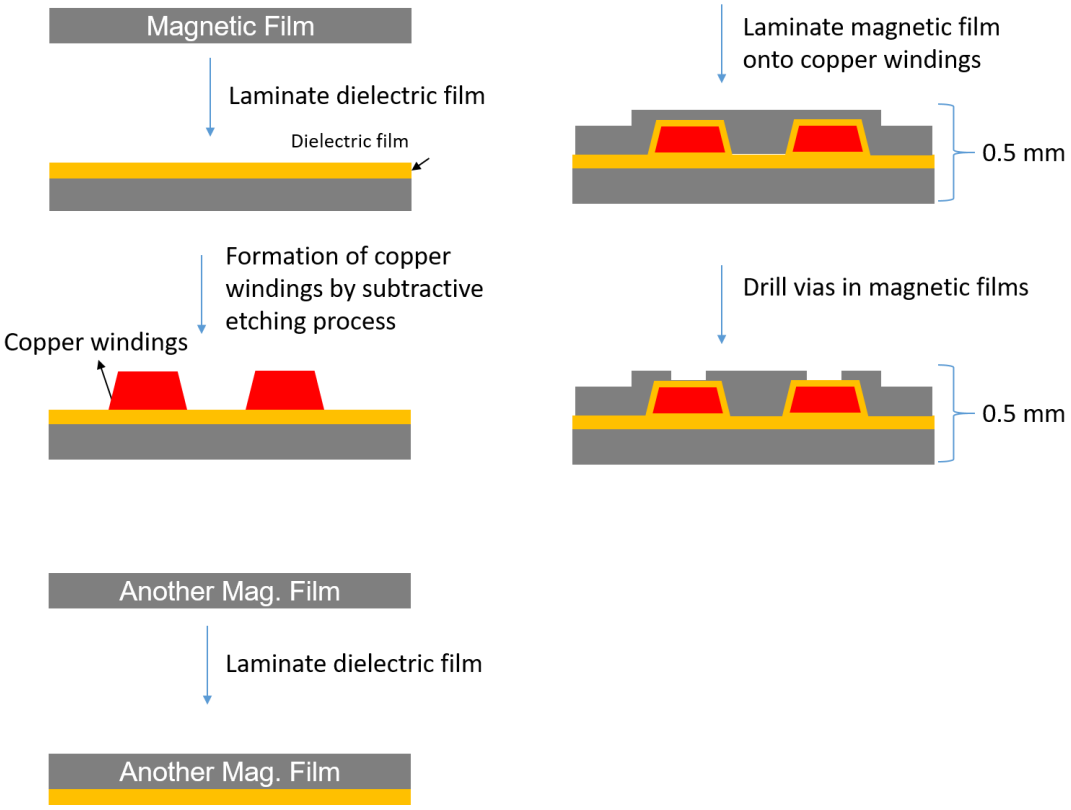

Figure 5.5: Fabrication process flow for planar inductor with magnetic cores.

Inductance as a function of frequency was characterized for the spiral inductors using a vector network analyzer (VNA) to study the effect of under-cut to inductance. The

structure of the fabricated spiral inductors are re-built in ANSYS, an electromagnetic simulation software. The measured and simulated inductance are plotted in Figure 5.6. The measured inductance shows a value of 100 nH while the simulated inductance shows a value of 90 nH. The fabricated inductors are cross-sectioned to analyze the effect of under-cut to inductance.

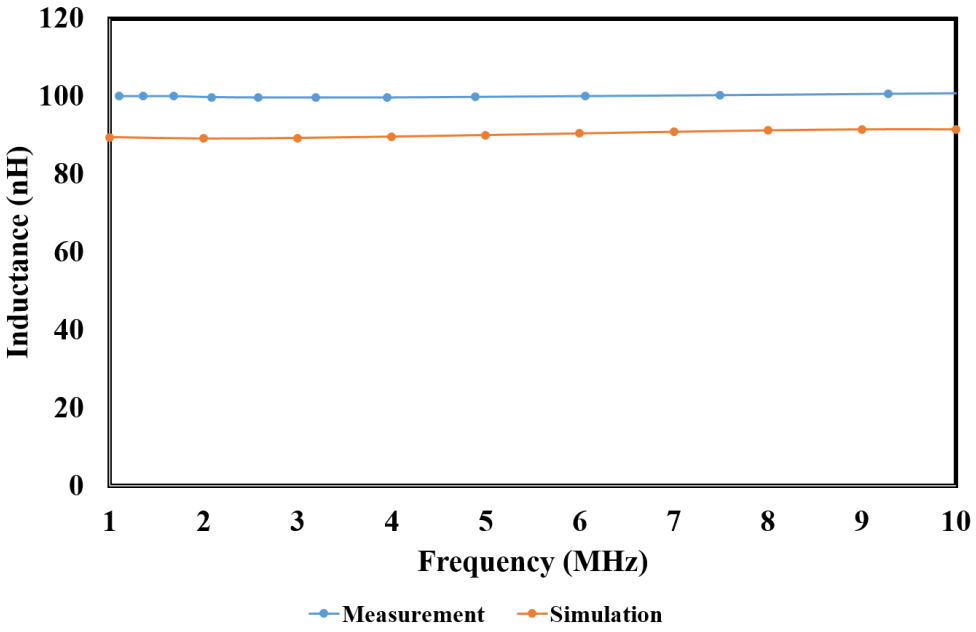

Figure 5.6: Inductance as a function of frequency

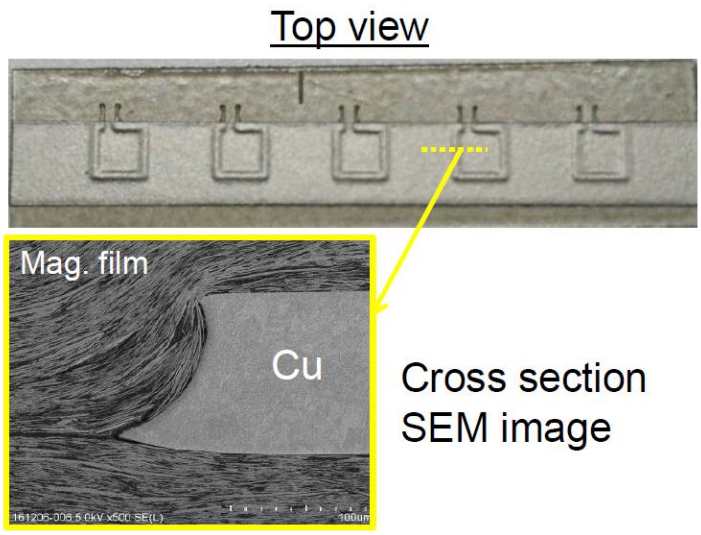

Figure 5.7: Top view and cross-section of fabricated spiral inductors using subtractive etching process (Courtesy to Nitto Denko).

Figure 5.7 shows the top-view and cross-section of the fabricated spiral inductors using subtractive etching process. The spiral inductors have one winding turn for low DC resistance. The copper windings are sandwiched between two high-permeability magnetic sheets for high inductance. The high inductance results from high-permeability magnetic metal-flakes as illustrated in the cross-section image. All the flakes are stacked layer-by-layer with the flake plane aligning along one direction. The under-cut is also observed from the cross-section image. Due to the under-cuts, the copper windings have a trapezoidal cross-section. The curved sides of the trapezoid support the alignment of the surrounding flakes. As a result, the high-permeability direction of flakes are aligned parallel with the direction of magnetic flux, rendering high inductance as explained in Figure 5.8.

If the spiral inductors were fabricated by semi-additive processes, a rectangular cross-section is expected. The steep sides cannot support the high-permeability direction of flakes to align parallel with the magnetic flux. As a result, the magnetic flux travels

thought low-permeability direction near winding sides, rendering low inductance as explained in Figure 5.8.

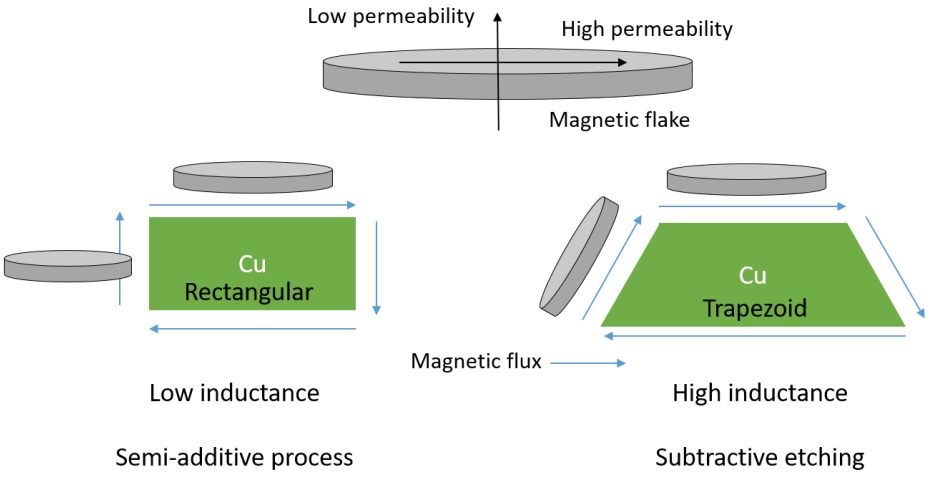

Figure 5.8: Effect of undercut on the inductance of inductors.

By using the developed process, the designed spiral inductors in Chapter 3 were fabricated and characterized. Figure 5.9 shows the top view and cross-section of the inductors. The inductor has one turn winding for low DC resistance. The size of the inductor is 9 mm^2 with a thickness of 80 μm. The copper winding is sandwiched between two 200 μm high-permeability magnetic sheets for high inductance.

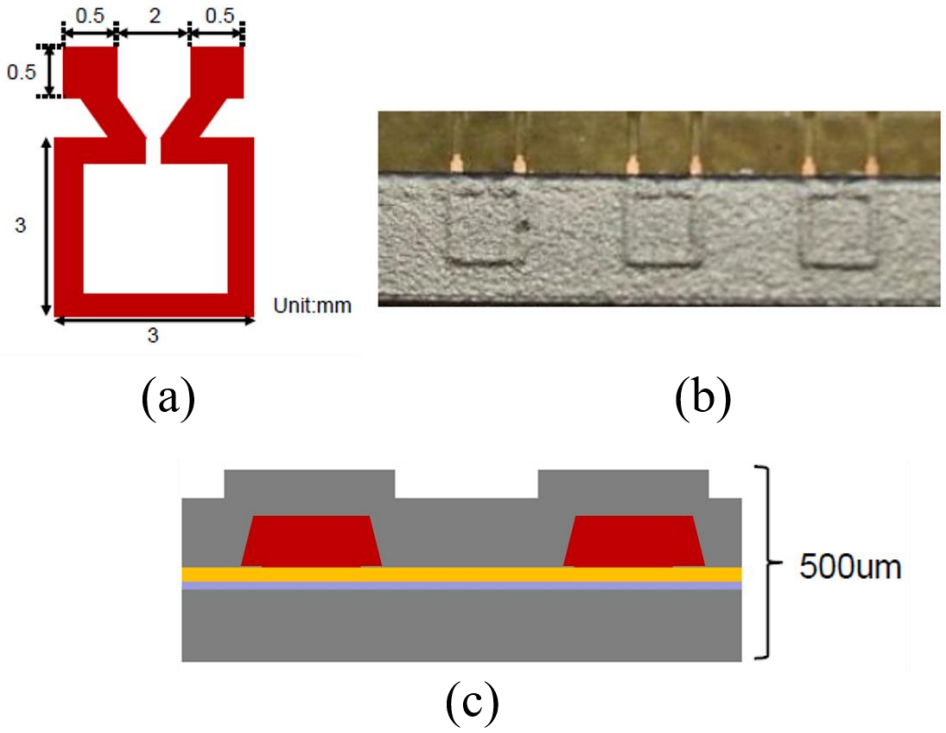

Figure 5.9: (a) Top view of the spiral inductors with copper windings only, (b) the top view of the spiral inductors with magnetic sheets, (c) the cross-section of the spiral inductors with magnetic sheets (Courtesy to Nitto Denko).

The frequency response of the fabricated inductors was characterized by using vector network analyzer (VNA). The characterization set-up is shown in Figure 5.10.

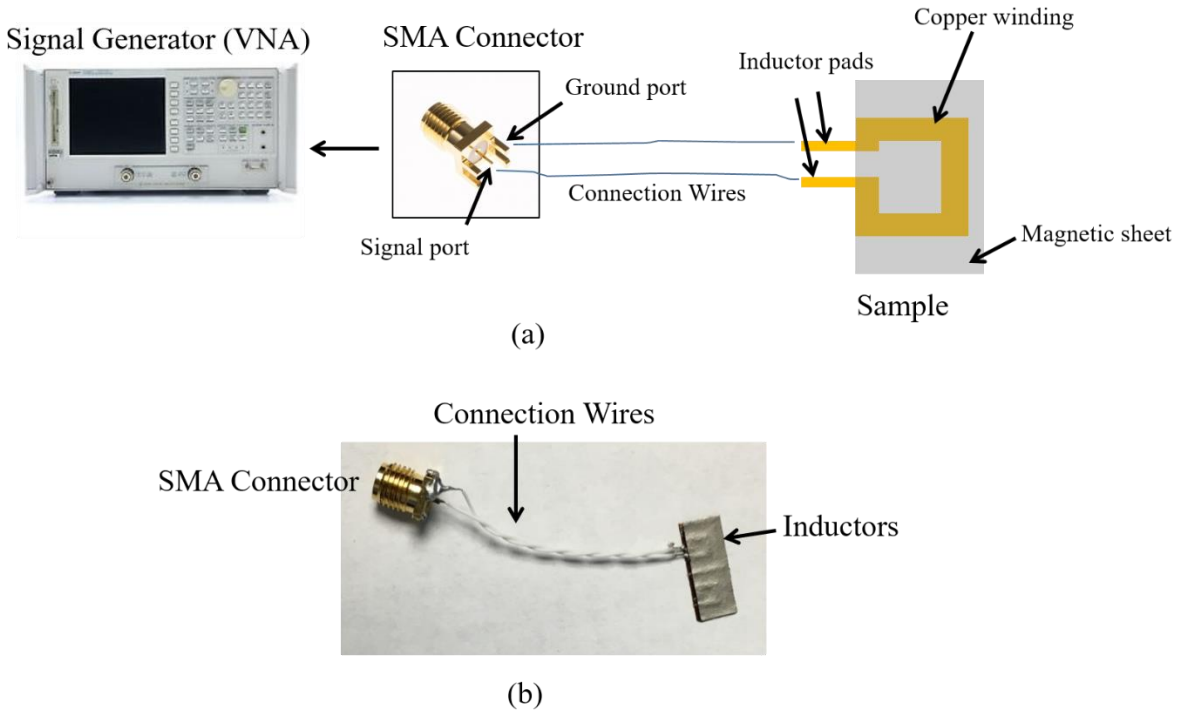

Figure 5.10: (a) Characterization set-up for inductance measurement at various frequency, (b) Picture of the measured spiral inductors

The set-up consists of three parts: sample, connection and signal generator. The signal generator, which is the VNA, generates AC signals with frequencies ranging from 1 to 10 MHz. The two inductor pads are connected to the ground and signal ports of the SMA connectors using long connection wires. The AC signal travels from the signal port to the inductor and return from ground port to the VNA. Y-parameter of the returned AC signal is measured to calculate the inductance by using (5.2

$$L = \frac{imag(\frac{1}{Y})}{2\pi f} \tag{5.2}$$

where Y is the measured Y-parameter, f is the frequency and L is the inductance. In order to accurately extract the inductance of the device-under-test, the inductance of the two

connection wires also need to be measured by the VNA with de-embedding structures. These de-embedding structures are necessary for accurate measurements. De-embedding structures have three parts, known as open, short and load. The function of the three de-embedding structures is to remove the effect of the parasitics from the two connecting wires and allow the VNA to solely measure the inductance from inductor. Figure 5.11 shows the de-embedding structures with open, short and load.

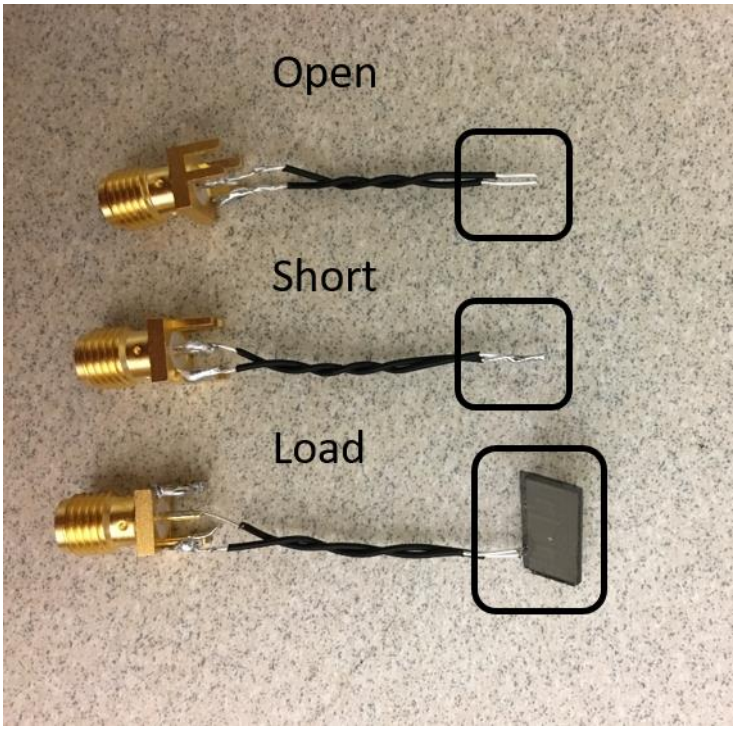

Figure 5.11: Photo image of de-embedding structures with open, short and load.

With the de-embedding structures, the Y parameter for inductors can be calculated as

$$\frac{1}{Y} = \frac{1}{Y_{LOAD} - Y_{OPEN}} - \frac{1}{Y_{SHORT} - Y_{OPEN}} \qquad \text{Equation 5.3}$$

where Y_{LOAD}, Y_{OPEN} and Y_{SHORT} are the measured Y parameters of load, open and short parts respectively. Figure 5.12 shows the measured inductance with and without using de-embedded structures. Without using the de-embedding structures, the measured inductance is sum of the inductance from connection wires and the inductance from inductors.

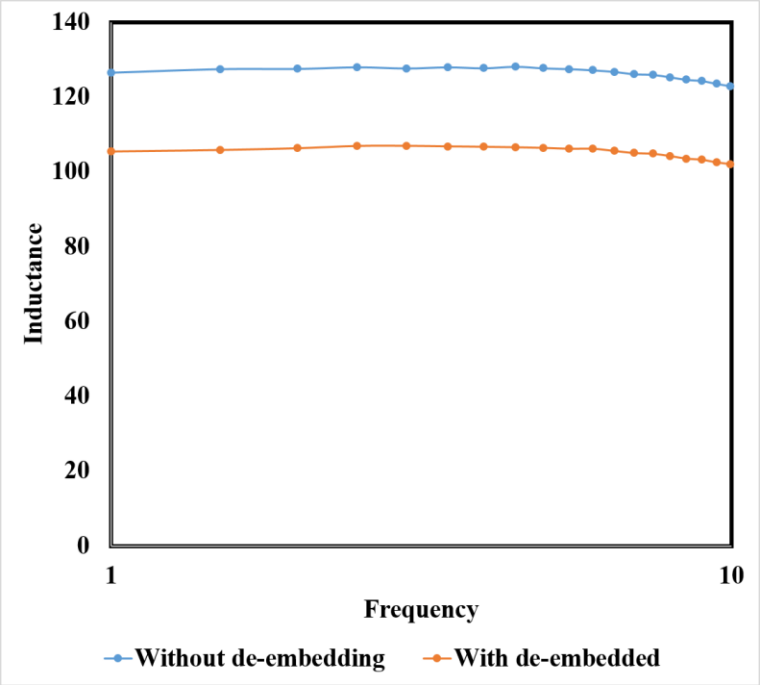

Figure 5.12: Measured inductance with and without using de-embedding structures

The measured inductance of designed inductors in Chapter 4 are plotted in Figure 5.13. The inductors with two high-permeability magnetic sheets show inductance of ~100 nH at 1 to 10 MHz. The magnetic sheet improves the inductance by a factor of 12.5X. Without magnetic sheets, the inductance is ~8 nH as shown in Figure 5.13.

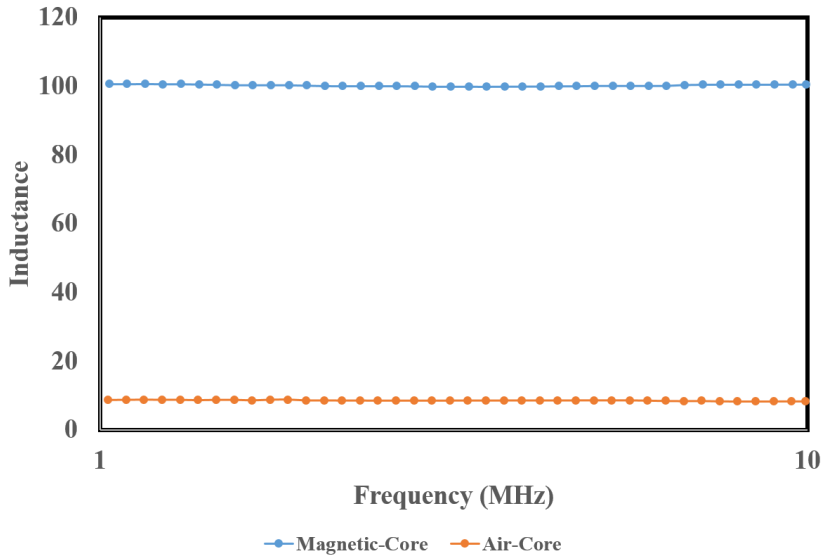

Figure 5.13: Measured inductance of inductors with magnetic sheets (magnetic-core) and without magnetic sheets (air-core)

The current response of the fabricated inductors was also measured by using VNA and DC bias-tee. The set-up is shown in Figure 5.14. The set-up shares similar tools as the aforementioned set-up for frequency response. The only difference is the generated signal. The set-up for current-response measurement generates a signal with two components, AC and DC. For frequency-response measurement, the generated signal only contains AC component. The DC signal is generated from a power source which applies constant current. The DC bias-tee combines DC signal from power source and AC signal from VNA and send the combined signal to the inductors. Inductance at 10 MHz was measured under various DC current. The results are plotted in Figure 5.15.

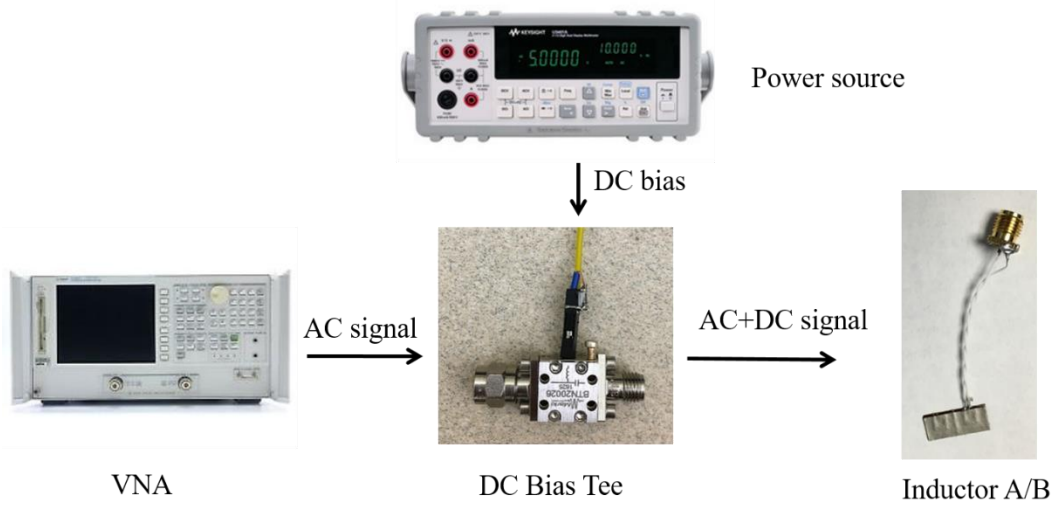

Figure 5.14 Characterization set-up for current-handling measurement

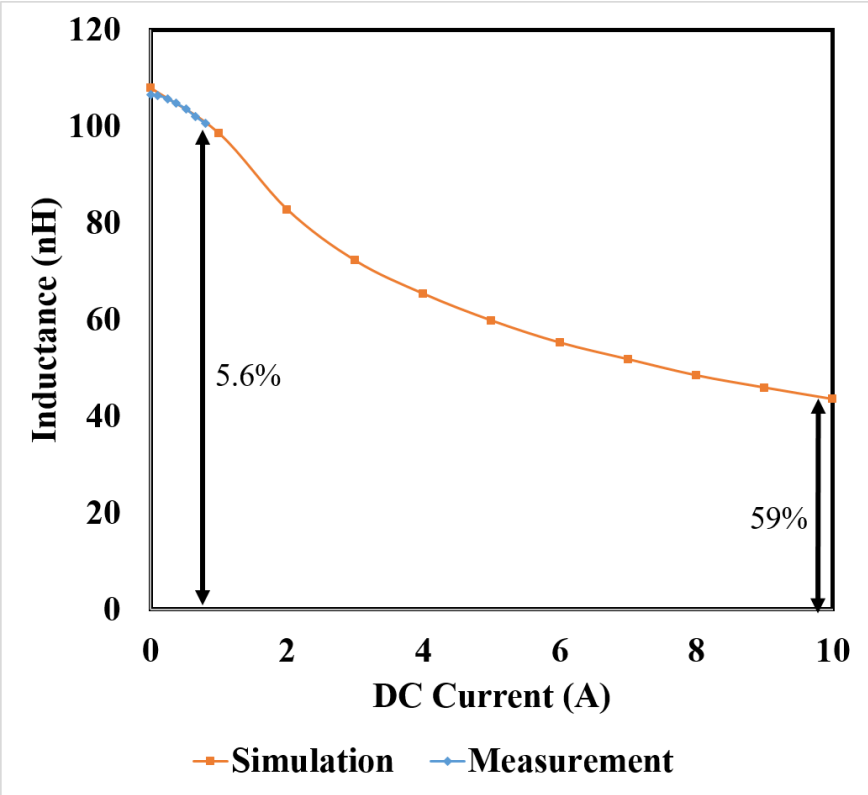

Figure 5.15: Measured and simulated inductance at 10 MHz with various DC bias.

A 5.6% drop in inductance is observed when the applied DC current increases from 0 to 0.8 A. The maximum applied DC current is limited by the DC bias tee. To capture the inductance at higher DC current, accurate models are necessary. By comparing the measurements with the simulations, an overlap between two lines is observed, indicating the accuracy of the FEM models. At 10 A, the fabricated inductors are expected to show 59% inductance drop. This reflects the low current-handling capability of spiral inductors. To handle more current, solenoid inductors were fabricated.

5.3 Cavity-embedded Solenoid Inductors

For solenoid inductors, a cavity-embedding approach was developed to fabricate and integrate solenoid inductors into substrates. The process flow is shown in in Figure 5.16. Single-bar solenoid inductors were first fabricated to evaluate the developed process. Since the structure of solenoid inductors require via-filling process, only semi-additive process is suitable for the structure. High-permeability magnetic sheets with thickness of 450 μm were first diced into small magnetic bars using a dicing saw. The size of the bars is 3x0.7 mm^2. Next, CO_2 laser-drilling was used to form cavities on 450 um thick organic substrates with 12 Watts applied power. The cavities have a size of 3.2x0.9 mm^2. Dielectric films of 0.1 mm thickness were then laminated onto the bottom side of the substrates at 100 ^oC and 0.3 MPa for 60s. The magnetic bars were picked and placed into the cavities. After placement, 0.1 mm thick dielectric films were laminated onto the top side of the organic substrates at at 100 ^oC and 0.3 MPa for 60s. The substrates were cured at 180 ^0C for 1 hour. UV laser-drilling were used to form vias with 6 Watts applied power. The metallized vias and windings were formed using the aforementioned semi-additive process.

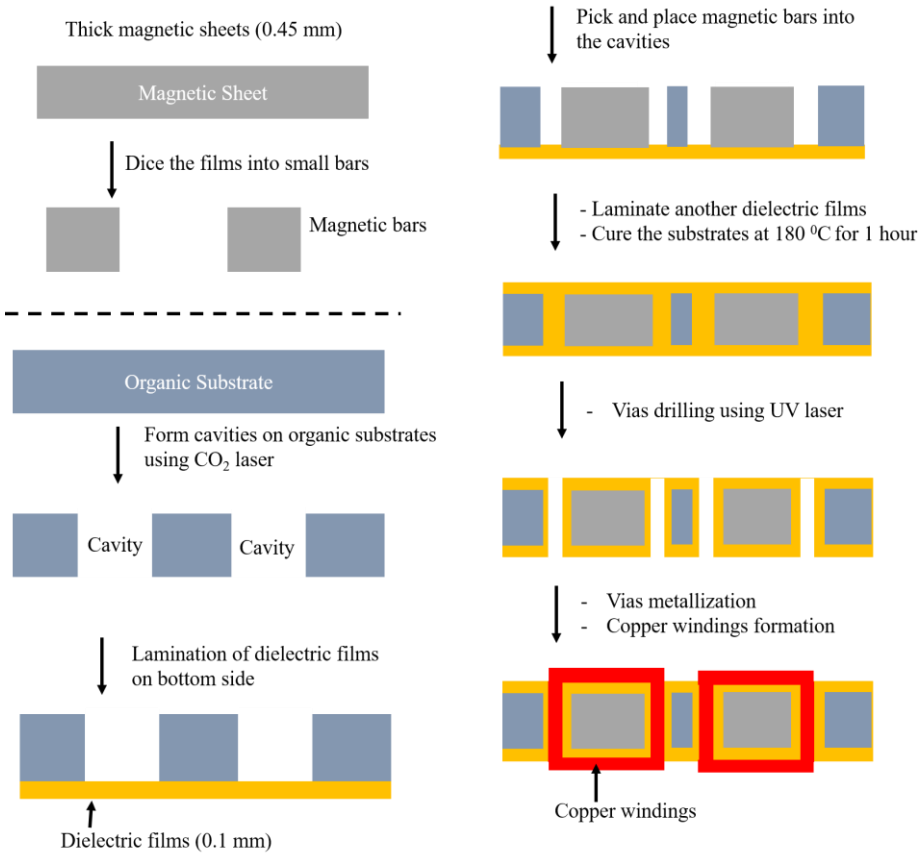

Figure 5.16: Fabrication process flow for solenoid inductors

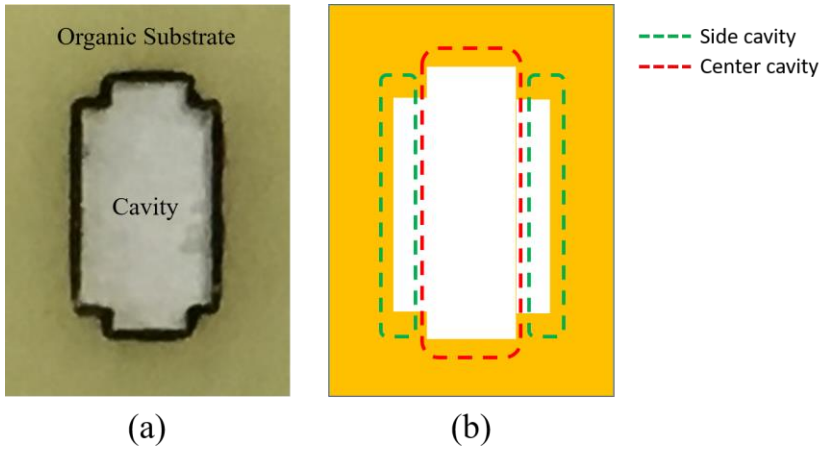

Figure 5.17: (a) Photo image of substrate with a cavity and (b) Schematic of substrate with a cavity.

Figure 5.17 presents top views of substrate with a cavity. The shape of the cavity is not a rectangular shape. It consists of two parts, one center rectangle and two side rectangles. The high-permeability bars are assembled into the center part. The two side-rectangles are designed for vias. With the two side-rectangles, vias can be laser-drilled into soft dielectric films that require less power. Without the two side-rectangles, vias need to be laser-drilled in organic substrates. The organic substrates consist of long glass fibers and epoxy resin, which makes it hard to drill vias in the substrates. Glass fibers need high laser-power to be processed while epoxy resin can be processed with low-power. If high drilling power is used, vias can have thermal damage, resulting in irregular shapes as shown in Figure 5.18. During the metallization process, the irregular shapes lead to reliability issues such as copper delamination. For low drilling power, the substrates cannot be drilled through.

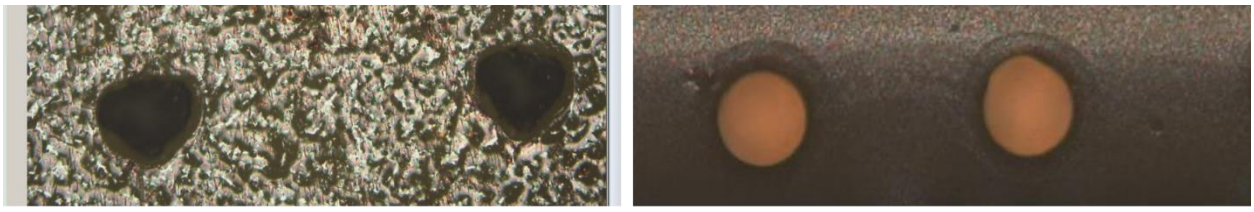

Figure 5.18: Laser-drilled vias on (a) organic substrates and (b) dielectric films.

Figure 5.19 shows the cross-section of the solenoid inductor. The outermost part is the organic substrate, which consists of epoxy resin and long glass fibers. The high-permeability magnetic bar is embedded in the center using dielectric films. The magnetic bar is surrounded by copper windings and copper vias.

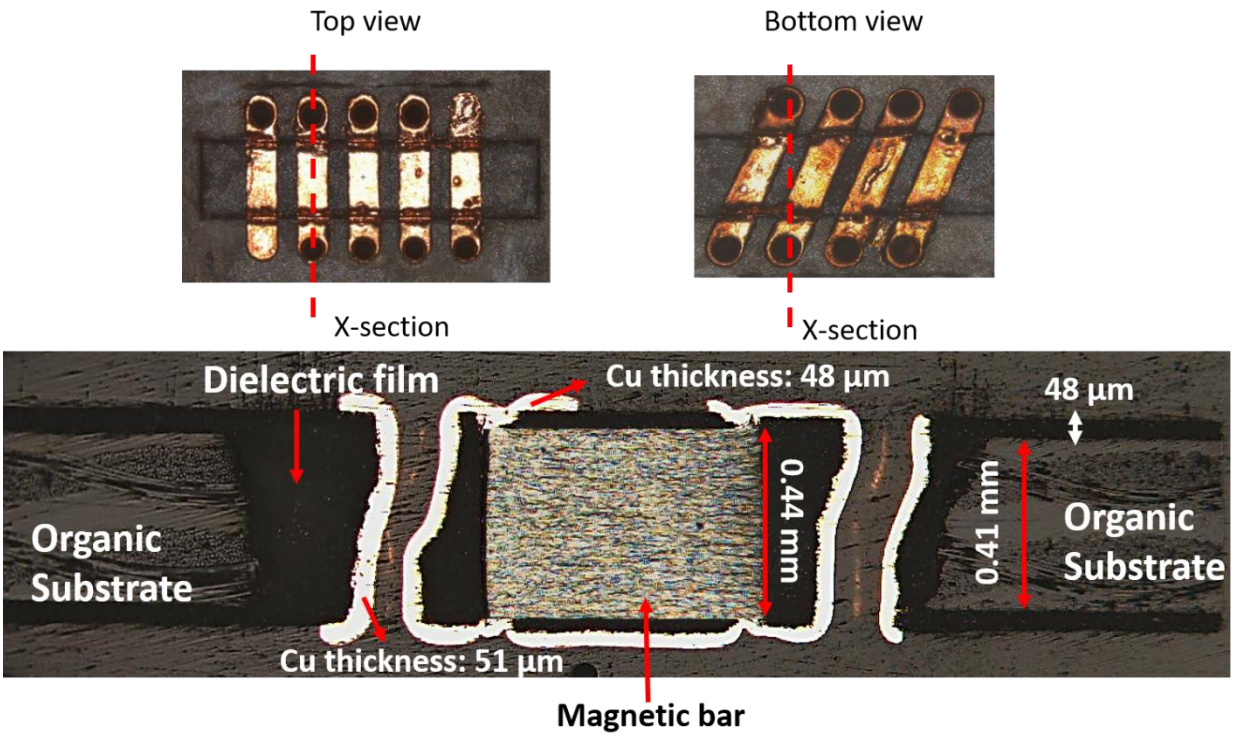

Figure 5.19: Cross-section of the solenoid inductors.

Several process challenges are observed from the cross section. First challenge is in the conformal vias. The solenoid inductors were designed to have completely-filled vias for low DC resistance. After electroplating for an hour, the large vias with diameters of ~300 µm cannot be filled, resulting in high DC resistance. It is possible to completely fill the vias with longer electroplating time. However, this approach requires electroplating solutions with specific additives that suppress the growth of copper on the surface and promotes the growth of copper inside the vias. Study of the special electroplating solution is beyond the scope of this research and is not discussed in here. One efficient way to completely fill the vias is to use copper paste, as shown in Figure 5.20.

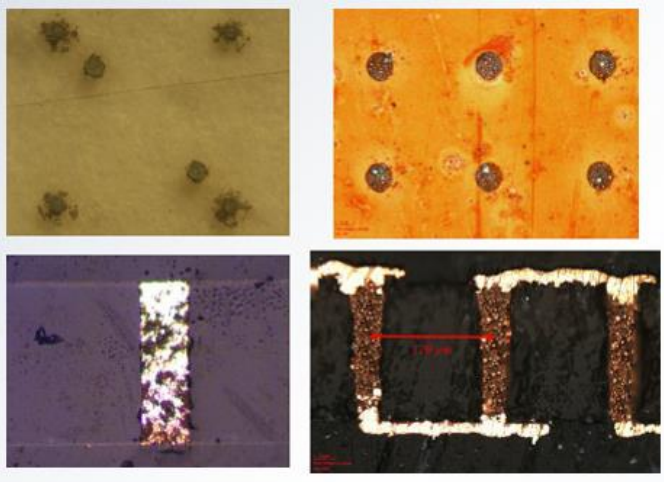

Figure 5.20: Top view and cross-section of vias filled with Cu paste. (Courtesy to Chintan Buch)

Second process challenge is the curved vias. During the via-drilling step, the process was designed to laser-drill from one side. However, because of high filler-content of the dielectric films, it was difficult to drill from one side. The high filler-content film was selected for the solenoid inductor process because of (1) high thermal conductivity of 4 W/mk and (2) small CTE of 15 ppm/^{0}C. As compared to organic substrates with thermal conductivity of 0.25 W/mk, the selected dielectric film can easily move dissipated heat of inductors away from substrates to alleviated thermal stress [54, 55]. With a CTE close to Fthe organic substrates, the high filler-content film also leaded to less warpage issue when it was integrated into packages.

To form vias in the dielectric film, two-side drilling was employed. Without alignment makes, it was difficult to precisely align the locations of vias from both sides, resulting in curved vias. Dielectric films with less filler or high-power laser can enable via-drilling from single side as shown in Figure 5.21.

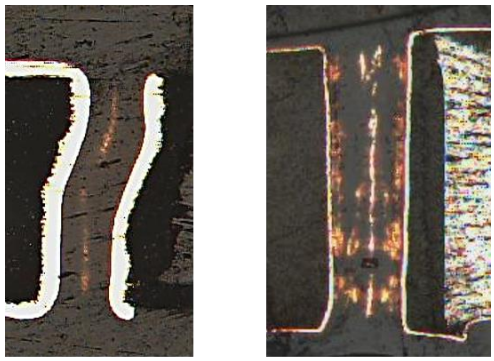

(a) (b)

Figure 5.21: (a) Curved via on dielectric film with high filler content, (b) Straight via on dielectric film with low filler content.

5.4 Chapter Summary

Fabrication and characterization of spiral and solenoid designs with advanced magnetic materials are presented in this chapter. Subtractive etching process is used to fabricate thick 2D copper windings in a short time. However, with high aspect ratio copper, it introduces under-cut problem, which can lead to higher DC resistance as compared to the designed value. The effect of under-cut on inductance is also studied. It turns out that the under-cut improves inductance of magnetic-core inductors. This only applies to magnetic cores which consisted of magnetic particles with anisotropic properties. On the other hand, semi-additive process does not have under-cut problem but needs additional process steps to form thick copper windings.

Two approaches, core-less and cavity-embedding, are employed to fabricate and integrate spiral and solenoid inductors with magnetic cores. The frequency response of inductance, current response of inductance and DC resistance are characterized for both types of inductors.

For magnetic-core spiral inductors, the measured inductor performance metric is 10 nH/mΩ. Without magnetic cores, a ~12X drop in inductance density is observed, indicating the importance of having magnetic cores. The measured DC resistance is ~10 mΩ. The measured value matches the designed value. For current handing, the magnetic-core spiral inductors show a 56% inductance drop at 10 A, indicating the low-current handing capability of the inductors.

For magnetic-core solenoid inductors, single-bar solenoid inductors are first fabricated to evaluate the developed process. Several process challenges such as via-filling and curved vias are observed from the cross sections. Solutions are proposed to address these challenges. With fully filled vias, the magnetic-core solenoid inductors are expected to have 13 A current handling and 10 nH/mΩ at a thickness of 600 μm.

CHAPTER 6. SUMMARY AND FUTURE WORK

6.1 Summary

Power supply is emerging as a major challenge in realizing future computing systems for both mobile processors because of the size restrictions, and in high-performance computing applications such as servers or data centers because of the need for high efficiency and performance. Power supply includes power conversion, power delivery and power management. Power converter topologies are mostly based on switching regulators that utilize inductors as the main storage components. The inductor size, performance and efficiency determines the overall power module size and performance in such cases. By incorporating advanced magnetic metal-polymer composites in the inductor cores, the thickness and lateral dimensions of inductors can be reduced without compromising electrical performance. With smaller form-factors, power modules can be integrated with substrates, resulting in granular power distribution that is optimized for specific voltage domains in the ICs, shorter power delivery network between modules and loads, and higher power delivery efficiency.

The objective of this research was to demonstrate miniaturized inductors with high current-handling and high efficiency for integrated power delivery. Three major tasks were identified to achieve: (1) thickness-scalable magnetic composites that can achieve high permeability with low loss in high frequencies, (2) inductor designs that can simultaneously achieve high inductance/R_{DC} and current-handling, and (3) inductor fabrication process to realize various optimized topologies.

Model and Design of Magnetic Composite

The objective of this task was to model and design thick magnetic composites with high permeability to achieve high efficiency of 10 - 20 nH/mΩ for inductors. Analytical models were developed to assist the design of magnetic composites with high permeability of ~141 and high-frequency stability upto 10 MHz. By adopting metal-polymer composite approach, thickness-scalable magnetic materials were achieved. Both the high permeability and large thickness gave rise to high inductance of 100 nH for the inductors with 10 mΩ resistance.

Based on the analytical models, two loss contributors, eddy-current loss and ferromagnetic resonance loss, were alleviated by designing the magnetic particles with flake morphology. The flakes with diameter of 40 um and thickness of 1 μm resulted in high in-plane permeability and low eddy current losses from small Z dimensions. The FMR was also pushed to 10 GHz with flake morphology. The low losses eventually leaded stability to magnetic composites at 1 – 10 MHz. The accuracy of the analytical models was proofed by the good correlation between measured and estimated permeability.

Model and Design of Inductors

The objective of this task was to model and design inductors with high current-handling of 10 – 20 A with a small footprint of 10 mm^2. Key parameters that were evaluated to achieve the desired objectives were polymer gaps between copper windings in the choice of inductor designs. Simulated results indicated that a 100 um thick polymer gap improved the current handling of spiral inductors from 3 A to 10 A because of the increased

reluctance of spiral inductors. However, the improvement came at a price of low L/R_{DC} of 6.5 nH/ mΩ due to the smaller inductance.

Without the need of polymer gaps, solenoid inductors showed both high current-handling capacity and high efficiency. For a 10 mm^2 area, the designed solenoid inductors showed a current-handling of 12 A, an efficiency of 10 nH/mΩ and a thickness of 600 μm. When integrated into substrates, solenoid inductors also showed good electromagnetic compatibility due to the constrained magnetic field inside substrates.

Fabrication and Integration of Designed Inductors

For this task, the objective was to develop a process to fabricate and integrate magnetic-core inductors into substrates to realize system miniaturization. For spiral inductors, a core-less approach was employed to achieve the objective. The approach directly built copper windings on thick magnetic sheets rather than organic substrates. The thick magnetic sheets were made strong enough to pass all substrate processes without failures. These core-less inductors achieved high inductance with a profile of 500 μm. The high inductance was caused by the alignment of magnetic flux parallel to the high-permeability direction of flakes.

For solenoid inductors, a cavity-embedding approach was employed to achieve the objective. Unique substrate-embedded inductors were accomplished by including the magnetic composites as a part of substrate. As compared to the standard surface-mounted technology, the cavity-embedding approach truly integrated inductors into substrates without adding any additional height to the system.

To realize the integrated inductors, thermal and mechanical considerations were also made to choose the dielectric materials with high thermal conductivity of 4 W/mk and small CTE of 15 ppm/^{0}C. The high thermal conductivity helped to move heat away from inductors to lower thermal stress while the small CTE reduced warpage issue. These integrated inductors achieved the targeted electrical performance with a profile of 600 μm and high reliability. For solenoid inductors, a combination of electroplating and paste-filling process were used to define the copper windings and fill the vias. The fully filled vias gave low resistance of 10 mΩ and high efficiency 10 nH/mΩ to the inductors.

6.2 Future Work

This research demonstrates substrate-integrated miniaturized inductors with high efficiency and high-current handling. The inductors show high efficiency of 10 nH/mΩ, high-current handling of 12 A and a low thickness of 500 μm. The demonstrated inductors can help migrate the power converters close to the processors, leading to lower losses, more efficient and granular power delivery. Magnetic materials with superior properties, advanced inductor designs and innovative embedding processes are the three critical enablers to realize these inductors. The power converter performance can be further enhanced with material, design and process advances. Following directions are suggested for future research in this area:

Magnetic Materials: In order to realize IVRs in thinner substrates, higher switching frequencies of >100 MHz will be utilized in the future. The inductor operation should correspondingly be optimized at those frequencies. Innovative magnetic metal-polymer

composites with optimized morphology are required to enhance the frequency stability much beyond 100 MHz.

Inductor Design: Innovative inductor structures with coupled toroid designs need to be explored to achieve better current-handling without the need for thick inductor cores.

Inductor Fabrication: Vias add DC resistance to solenoid inductors. Challenges with conformal vias need to be addressed before fabricating any inductor structures that require vias. Filling the vias with conductive paste is one potential solution to address the challenge. However, the residual porosity, high stresses and incompatible sintering temperatures causes other challenges to the inductor fabrication and prevent the use of conductive paste. The feasibility of various via-filling options need to be further studied.

REFERENCES

[1] R. Tummala, V. Sundaram, P. M. Raj, and V. Smet, "Future of embedding and fan-out technologies," in Microelectronics Symposium (Pan Pacific), 2017 Pan Pacific, 2017, pp. 1-9.

[2] Murata LXFC series. Available: http://www.murata.com/en-us/about/newsroom/news/product/capacitor/2009/1005b

[3] Samsung Embedded MLCC Capacitors. Available: http://www.samsungsem.com/global/product/passive-component/mlcc/embedded/index.jsp

[4] C. Bunel, "ipdia: The 3D silicon leader," in 2016 International Symposium on 3D Power Electronics Integration and Manufacturing (3D-PEIM), 2016, pp. 1-15.

[5] E. A. Burton, G. Schrom, F. Paillet, J. Douglas, W. J. Lambert, K. Radhakrishnan, et al., "FIVR — Fully integrated voltage regulators on 4th generation Intel® Core™ SoCs," in 2014 IEEE Applied Power Electronics Conference and Exposition - APEC 2014, 2014, pp. 432-439.

[6] µDCDC Converters [Online]. Available: https://www.murata.com/~/media/webrenewal/campaign/ads/america/udcdc/lxdc_product_brief.ashx?la=en-us

[7] C. Ó. Mathúna, N. Wang, S. Kulkarni, and S. Roy, "Review of integrated magnetics for power supply on chip (PwrSoC)," IEEE Transactions on Power Electronics, vol. 27, pp. 4799-4816, 2012.

[8] M. A. Swihart, "Inductor cores–material and shape choices," Magnetics®-www. mag-inc. com, 2004.

[9] D. Mishra, "Modeling, design, fabrication and demonstration of multilayered ferromagnetic polymer-dielectric composites for ultra-thin high-denisty power inductors," Georgia Institute of Technology, 2015.

[10] S. Kulkarni, "Power supply on chip for high frqquency integrated volatge regulation," in APEC, Charlotte, North Caroline, 2015.

[11] D. S. Mathew and R.-S. Juang, "An overview of the structure and magnetism of spinel ferrite nanoparticles and their synthesis in microemulsions," Chemical Engineering Journal, vol. 129, pp. 51-65, 2007.

[12] M. S. Rylko, K. J. Hartnett, J. G. Hayes, and M. G. Egan, "Magnetic material selection for high power high frequency inductors in dc-dc converters," in Applied Power Electronics Conference and Exposition, 2009. APEC 2009. Twenty-Fourth Annual IEEE, 2009, pp. 2043-2049.

[13] H. Shokrollahi and K. Janghorban, "Influence of additives on the magnetic properties, microstructure and densification of Mn–Zn soft ferrites," Materials Science and Engineering: B, vol. 141, pp. 91-107, 2007.

[14] "Ferrites: Low losses at high frequencies," ed: TDK Corporation, 2017.

[15] L. Hitachi Metals America, "Amorphous & Nanocrystalline," ed, 2017.

[16] F. Kong, C. Chang, A. Inoue, E. Shalaan, and F. Al-Marzouki, "Fe-based amorphous soft magnetic alloys with high saturation magnetization and good bending ductility," Journal of Alloys and Compounds, vol. 615, pp. 163-166, 2014.

[17] H. Gavrila and V. Ionita, "Crystalline and amorphous soft magnetic materials and their applications- status of art and challenges," Journal of Optoelectronics and Advanced Materials(Romania), vol. 4, pp. 173-192, 2002.

[18] C. Tsai, B. Li, K. Jean, and C. Lin, "The effect of annealing on magnetic properties of iron-base amorphous alloy ribbons," Journal of Applied Physics, vol. 67, pp. 5586-5588, 1990.

[19] Y. Liu, Y. Yi, W. Shao, and Y. Shao, "Microstructure and magnetic properties of soft magnetic powder cores of amorphous and nanocrystalline alloys," Journal of Magnetism and Magnetic Materials, vol. 330, pp. 119-133, 2013.

[20] N. Wang, T. O'Donnell, S. Roy, M. Brunet, P. McCloskey, and S. C. O'Mathuna, "High-frequency micro-machined power inductors," Journal of Magnetism and Magnetic Materials, vol. 290-291, pp. 1347-1350, 2005/04/01/ 2005.

[21] N. Wang, T. O'Donnell, S. Roy, P. McCloskey, and C. O'Mathuna, "Micro-inductors integrated on silicon for power supply on chip," Journal of Magnetism and Magnetic Materials, vol. 316, pp. e233-e237, 2007/09/01/ 2007.

[22] R. Meere, T. O. Donnell, N. Wang, N. Achotte, S. Kulkarni, and S. C. O. Mathuna, "Size and Performance Tradeoffs in Micro-Inductors for High Frequency DC-DC Conversion," IEEE Transactions on Magnetics, vol. 45, pp. 4234-4237, 2009.

[23] T. O'Donnell, N. Wang, S. Kulkarni, R. Meere, F. M. F. Rhen, S. Roy, et al., "High Efficiency Micro-inductors on Silicon," in International Workshop on Power Supply On Chip (PwrSoC) 2008.

[24] K. Kawano and J. Nakajima. (2014, Dec 22). Material advances enable new power inductors. Available: https://www.electronicproducts.com/Passive_Components/Magnetics_Inductors_Transformers/Material_advances_enable_new_power_inductors.aspx

[25] X. De-Sheng, L. Fa-Shen, F. Xiao-Long, and W. Fu-Sheng, "Bianisotropy picture of higher permeability at higher frequencies," Chinese Physics Letters, vol. 25, p. 4120, 2008.

[26] J. L. Snoek, "Dispersion and absorption in magnetic ferrites at frequencies above one Mc/s," Physica, vol. 14, pp. 207-217, 1948/05/01/ 1948.

[27] P. M. Raj, D. Mishra, H. Sharma, M. Swaminathan, and R. Tummala, "Nanomagnetic Materials and Structures, and their Applications in Integrated RF and Power Modules," in Nanomagnetism, J. M. G. Estevez, Ed., ed: One Central Press (OCP), 2014, pp. 13-16.

[28] I. Iakubov, A. Lagarkov, A. Osipov, S. Maklakov, K. Rozanov, I. Ryzhikov, et al., "A laminate of ferromagnetic films with high effective permeability at high frequencies," AIP Advances, vol. 4, p. 107143, 2014.

[29] P. R. Morrow, C. M. Park, H. W. Koertzen, and J. T. DiBene, "Design and Fabrication of On-Chip Coupled Inductors Integrated With Magnetic Material for Voltage Regulators," IEEE Transactions on Magnetics, vol. 47, pp. 1678-1686, 2011.

[30] D. S. Gardner, G. Schrom, P. Hazucha, F. Paillet, T. Karnik, S. Borkar, et al., "Integrated on-chip inductors using magnetic material (invited)," Journal of Applied Physics, vol. 103, p. 07E927, 2008.

[31] K. H. Kim, J. Kim, H. J. Kim, S. H. Han, and H. J. Kim, "A megahertz switching DC/DC converter using FeBN thin film inductor," IEEE Transactions on Magnetics, vol. 38, pp. 3162-3164, 2002.

[32] D. Yao, C. G. Levey, R. Tian, and C. R. Sullivan, "Microfabricated V-Groove Power Inductors Using Multilayer Co-Zr-O Thin Films for Very-High-Frequency DC-DC Converters," IEEE Transactions on Power Electronics, vol. 28, pp. 4384-4394, 2013.

[33] N. Sturcken, "Thin Film Inductors for Integrated Power Conversion," in APEC, Tampa, FL, 2017.

[34] N. Sturcken, R. Davies, H. Wu, M. Lekas, K. Shepard, K. W. Cheng, et al., "Magnetic thin-film inductors for monolithic integration with CMOS," in 2015 IEEE International Electron Devices Meeting (IEDM), 2015, pp. 11.4.1-11.4.4.

[35] A. Hindmarch, D. Arena, K. Dempsey, M. Henini, and C. Marrows, "Influence of deposition field on the magnetic anisotropy in epitaxial Co 70 Fe 30 films on GaAs (001)," Physical Review B, vol. 81, p. 100407, 2010.

[36] C. R. Sullivan, J. Qiu, D. V. Harburg, and C. G. Levey, "Batch fabrication of radial anisotropy toroidal inductors," in 2016 International Symposium on 3D Power Electronics Integration and Manufacturing (3D-PEIM), 2016, pp. 1-15.

[37] J. Qiu and C. R. Sullivan, "Radial-Anisotropy Thin-Film Magnetic Material for High-Power-Density Toroidal Inductors," in 2012 7th International Conference on Integrated Power Electronics Systems (CIPS), 2012, pp. 1-6.

[38] K. Santosh, "PwrSOC Pasives-Inegrated magnetics," in IEEE APEC, Charlotte North Caroline, 2015.

[39] H. Song, "Soft Magnetic Composites for High Frequency Applications," 2015.

[40] R. Ramprasad, P. Zurcher, M. Petras, M. Miller, and P. Renaud, "Magnetic properties of metallic ferromagnetic nanoparticle composites," Journal of applied physics, vol. 96, pp. 519-529, 2004.

[41] C. Kittel, "On the theory of ferromagnetic resonance absorption," Physical Review, vol. 73, p. 155, 1948.

[42] C. Kittel, "Ferromagnetic resonance," Journal de Physique et le Radium, vol. 12, pp. 291-302, 1951.

[43] B. Lu, X. Dong, H. Huang, X. Zhang, X. Zhu, J. Lei, et al., "Microwave absorption properties of the core/shell-type iron and nickel nanoparticles," Journal of magnetism and magnetic materials, vol. 320, pp. 1106-1111, 2008.

[44] E. P. Wohlfarth, Ferromagnetic materials: a handbook on the properties of magnetically ordered substances vol. 2: Elsevier, 1980.

[45] T. Instruments, "Switching Regulator Fundamentals," ed: Texas Instruments, 2016.

[46] V. Bulovic, R. Ram, S. Leeb, J. Lang, and Y. Gu. (2001). 6.007 Electromagnetic Energy: From Motors to Lasers. Available: https://ocw.mit.edu

[47] Z. Zhang, "Coupled-inductor magnetics in power electronics," California Institute of Technology, 1987.

[48] E. Wang. Current Ripple Factor of a Buck Converter [Online].

[49] T. Eichhorn. Estimate Inductor Losses Easily in Power Supply Designs [Online].

[50] Introduction the WE-PDF Flatwire Inductor Series [Online].

[51] R. Ridley. (2005) Proximity Loss in Magnetics Wingings. Switching Power Magazine. 1-9.

[52] C. O. Mathuna, J. A. Cobos, S. Kulkarni, and B. Allard, "Power Supply on Chip for High Frequency Integrated Vltage Regulation," in IEEE APEC Charlotte, North Caroline, 2015.

[53] A. Renbi, A. Risseh, R. Qvarnström, and J. Delsing, "Impact of etch factor on characteristic impedance, crosstalk and board density," in International Symposium on Microelectronics, 2012, pp. 000312-000317.

[54] P. Klouda, "Thermally Conductive Printed Circuit Board Materials " in Components, Packaging & Manufacturing Technology Society, 2004.

[55] Carrying the Heat Away from Power Module PCB Designs [Online].